

CRYSTALLINE-SILICON/ORGANIC
HETEROJUNCTIONS FOR SOLAR
PHOTOVOLTAICS

SUSHOBHAN AVASTHI

A DISSERTATION
PRESENTED TO THE FACULTY
OF PRINCETON UNIVERSITY
IN CANDIDACY FOR THE DEGREE
OF DOCTOR OF PHILOSOPHY

RECOMMENDED FOR ACCEPTANCE
BY THE DEPARTMENT OF
ELECTRICAL ENGINEERING
ADVISER: JAMES C. STURM

NOVEMBER 2011

© Copyright by Sushobhan Avasthi, 2011.

All Rights Reserved

Abstract

Solar cells based on crystalline silicon offer high efficiency but they are expensive due to the high temperatures required in their fabrication. The alternative approach using low-temperature processable organic-semiconductors is potentially cheaper, but the organic solar cells are not very efficient. In this thesis we explore if organic semiconductors can be integrated with silicon to form hybrid organic/silicon solar cells that are both efficient and low-cost. Specifically, we demonstrate that a) organic molecules can be used to reduce carrier recombination at the silicon (100) surface and b) a solution-processed organic/silicon heterojunction can replace the conventional silicon p-n junction to yield solar cells with high power conversion efficiencies ($>10\%$).

With decreasing wafer thicknesses and improving bulk lifetimes of silicon solar cells, losses due to carrier recombination at the silicon surface are becoming increasingly important. At a bare silicon surface, some of the silicon valencies remain unsatisfied. These “dangling-bonds” cause midgap states at the silicon surface where photogenerated carriers can recombine, resulting in lower performance. Typically, a layer of silicon oxide/nitride is deposited on the silicon, at high-temperatures ($>350\text{ }^\circ\text{C}$), to passivate the dangling-bonds and reduce surface recombination. Organic semiconductors can be deposited at much lower temperatures, but in general organic materials do not react with the silicon dangling-bonds and the surface remains unpassivated. In this work, we demonstrate that the organic molecule 9,10 phenanthrenequinone (PQ) reacts with and satisfies the silicon dangling bonds, leading to a relatively defect-free silicon surface with a very low surface recombination velocity (150 cm/s). Electrical measurements of the metal/insulator/silicon devices show that the Fermi-level at the PQ-passivated silicon surface can be modulated and an inversion layer can be induced in silicon. High electron mobility of $600\text{ cm}^2/\text{Vs}$ is measured at the Si/PQ interface further proving the electronic quality of the PQ-passivated surfaces.

To generate a photovoltage in a solar cell, the photogenerated carriers need to be spatially separated at two electrodes of opposite polarity. In solar cells this is typically accomplished using a p-n junction. While the p-n junction technology is well understood, the fabrication of p-n junctions on silicon is an expensive process because it requires ultra-clean furnaces, pure precursors and high temperatures. In this thesis we successfully replace the silicon p-n junction with an silicon/poly(3-hexylthiophene) heterojunction that can be manufactured at low temperatures ($<150\text{ }^{\circ}\text{C}$) with a simple spin-coating process. The key design rules to achieve a high quantum-efficiency and high open-circuit voltage are discussed and experimentally demonstrated. Finally we highlight the importance of reducing minority-carrier currents in these heterojunction devices, which gives a pathway for further improving the efficiency of heterojunction solar cells. Using the prescribed design rules and optimizing device structure, a silicon/organic heterojunction solar cell with an open-circuit voltage of 0.59 V and power conversion efficiency of 10.1 % is demonstrated.

Acknowledgements

First, I would like to thank my adviser, Professor James C. Sturm, for his guidance and support. I am especially thankful for his encouraging words, without which I could not have endured the countless paper rejections, months of fruitless toil and moments of doubt. I am very thankful to Professor Claire Gmachl and Professor Antoine Kahn for taking the time to read this thesis and provide valuable comments. I am also very thankful to Professor Sigurd Wagner and Professor Steve Lyon for the many stimulating discussions we have shared over the last six years.

This work is part of an interdisciplinary project that spanned three academic departments and four research groups. I would be remiss not to acknowledge the contribution of my collaborators. The work presented in Chapter 3 was guided by Professor Jeffrey Schwartz of the Department of Chemistry. I must thank Dr. Grigory Vertelov and Will McClain for patiently helping an electrical engineer understand chemistry. Once again, a big note of thanks goes to Professor Antoine Kahn of the Department of Electrical Engineering for his guidance in designing the surface science experiments detailed in Chapter 3 and Chapter 5. I am especially grateful to Dr. Yabing Qi and Dr. Zelei Guan for actually conducting the surface science experiments, which often required investment of considerable time and energy. Finally I must acknowledge Professor Lynn Loo of the Department of Chemical Engineering and her research group for helping setup the experiments described in Chapter 5. These experiments could not have been successful without the generous help from Rich Fiorillo, He Wang, Dr. Jongbok Kim, and most importantly Stephanie Lee.

I must also acknowledge the generosity of all the funding agencies. The work in this theses was supported by the Princeton University graduate fellowship, and the National Science Foundation under grants (DMR-1005892) and the Princeton MRSEC (DMR-0819860).

A special thanks goes to all members in Sturm group. First I must thank the senior

members, Keith H. Chung, Weiwei Zheng, Kun Yao, and Bahman Hekmatshoar, for mentoring me. I also commend Jiun-Yun Li, Chiao-Ti Huang, Ken Nagamatsu, Yifei Huang, Ting Liu, Noah Jafferis, Bhadrinarayana L. Visweswaran, Warren Rieutort-Louis, Josue Sanz-Robinson, Joseph D’Silva, and Amy Wu, for excellent camaraderie and cooperation. In the wider Department community, intellectual discussions with Jianhua He, Wenzhe Cao, and Dr. Igor Trofimov, were very helpful.

My gratitude also goes to the staff at the Department of Electrical Engineering and PRISM, who work tirelessly in the background. I am especially indebted to Joe Palmer and Mike Gaevski for always making the time for me, no matter how short a notice. Same goes for Dr. George Watson, Dr. Conrad Silvestre, and Dr. Nan Yao, who have always been a door-knock away. Ms. Carolyn Arnesen and Ms. Sheila Gunning, I thank you for your consideration and attention. Finally, a special note of thanks to Ms. Sarah M. McGovern - There never was a bureaucratic snafu that Sarah could not sort while maintaining an infectious smile.

In my first week at Princeton I was told that one does not complete a PhD by oneself. Standing on the verge of earning one, I cannot agree more. I was blessed with an absolutely fabulous circle of friends whose contribution towards my success cannot be overstated. Shyam, Abhishek and Madhur you guys are my counsels and my confidants. You are family and it has been my pleasure getting to know you better. Deep, I still miss our late-night conversations. Lorne, thank you for your outrageous laughter and uplifting guitar solos. Kevin, my only regret is that I did not get to know you earlier but hopefully our paths shall cross again. Tanushree and Sibren, you are the most welcoming and honest couple I have ever had the pleasure of knowing and I hope we continue to enjoy board games and “poori-making” sessions together. A very warm note of thanks to Anuradha, Andrea, Gonzalo, Prateek, Eugene, Saurabh, Chiranjeev (CJ), Seshadri, Prashant & Divya, Raghu, Zubin, and Gitanjali. Meghna and Jiji, thank you for all the support. Finally a shout out for two of the most

important people in my life. Aman, you are my best friend, my shrink, my rock, so a simple thank you is not enough but I will say that I could not have navigated the ups and downs of PhD without you. Stephanie, we met during a particularly low point in my PhD but you decided to walk with me anyways. I am unable to express the full depth of my feelings in a sentence so for now I will just say this - my life has been infinitely richer because you are in it.

In the end, I want to acknowledge my family. First, I must thank my parents. They have always supported me, cared for me, and have never shied away from sacrificing their own happiness for my benefit. Ma and Papa, this is to you. My younger brother, Suvats, has always overlooked my failings and has been there for me. He keeps me honest and grounded, and for that I am eternally grateful. I was fortunate to grow up in a large and very loving joint family of ten members and a lot of my character has been molded by my aunts and uncles. My aunts, Badi-Bua, Sirf-Bua and Choti-Bua, are the source for everything I know about creativity, aesthetics, and patience. My uncles, Bade-Chacha and Chote-Chacha, taught me by example the importance of discipline and commitment. I would also like to thank my maternal uncles and their families, specifically Chote-mama, Chote-mami and Prashant. To a young fresh-off-the-boat graduate, you were a home away from home. While I am slightly headstrong and bad at keeping in touch, I shall never forget all that you have done to make my stay in the US more than comfortable. Finally, I must express my gratitude to my grandparents. For all practical purposes, I was raised by my grandmothers and I can honestly say that no one shall ever love me as unconditionally they do. In all my academic pursuits, including the PhD, I have been following in the footsteps of my grandfathers. They were my first and most important teachers, and as I stand to receive my final degree their absence is my only regret.

To my grandparents

Contents

Abstract	iii
Acknowledgements	v
List of Tables	xv
List of Figures	xvii
1 Introduction	1
1.1 Motivation	1
1.2 This Work	3
1.3 Solar Cells: Basics	5
1.4 Efficiency of Silicon Solar Cells	6
1.4.1 Short-Circuit Current	7
1.4.2 Fill-Factor	9
1.4.3 Open-Circuit Voltage	10
1.5 Methods to Reduce J_0 : Back Surface Fields	12
1.5.1 Reducing Bulk Recombination	12
1.5.2 Reducing Surface Recombination	13
1.6 Previous Work	16
1.6.1 PERL Cell: Representative n^+ - p - p^+ Homojunction Solar Cell	16
1.6.2 HIT Cell: Representative p^+ - n - n^+ Heterojunction Solar Cell .	18
1.7 Thesis Outline	20

2	Silicon/Organic Heterojunctions for Photovoltaics	24
2.1	Introduction	24
2.2	Fundamental Band Requirements of Silicon/Organic Wide-Bandgap Heterojunctions	26
2.3	Silicon/Organic Interface: Issues and Solutions	28
2.3.1	Problem 1: Band-Alignment	28
2.3.2	Problem 2: Surface defects	30
2.4	Silicon/Organic Heterojunction to Block Minority Carriers at the Anode	33
2.4.1	Closed-Form Expression of Minority Carrier Current in Hetero- junction	34
2.5	Silicon/Organic Heterojunction to Block Majority Carriers at Anode	37
2.5.1	Closed-Form Expression of Majority Carrier Current in Hetero- junction	39
2.6	Conclusion	43
3	Silicon Surface Passivation by 9,10-Phenanthrenequinone	45
3.1	Introduction	45
3.2	Comparison with Other Passivation Schemes	46
3.3	Materials and Equipment	47
3.4	Minority Carrier Lifetime Measurement	48
3.4.1	Effect of Surface Recombination	49
3.4.2	Quasi Steady-State Photoconductance Decay	49
3.4.3	Relation Between s and $\tau_{surface}$	51
3.5	Silicon Surface Passivation by Wet Chemicals	53
3.6	Silicon Surface Passivation by 9-10 Phenanthrenequinone	55
3.6.1	Method	55
3.6.2	Surface Recombination at the Si/PQ Surface	56
3.6.3	Spectroscopic Analysis of the Si/PQ Interface	59

3.7	Field-Effect Devices	69
3.7.1	Metal-Insulator-Semiconductor Capacitor	69
3.7.2	Metal-Insulator-Semiconductor Field-Effect Transistor	70
3.8	Conclusion	76
4	Silicon/Organic Heterojunction to Block Minority Carriers	78
4.1	Introduction	78
4.2	Proof of Concept: Simulations	80
4.3	Probe of Minority Carrier Current	82
4.3.1	Design	83
4.3.2	Fabrication	86
4.3.3	Characterization	87
4.4	Reduced Minority Carrier Recombination at the P-type Contact	96
4.4.1	Materials and Fabrication	97
4.4.2	PQ-passivated Si/TPD Heterojunction	97
4.5	Conclusion	101
5	Silicon/Organic Heterojunction to Block Majority Carriers	103
5.1	Introduction	103
5.2	Proof of Concept: Simulations	104
5.3	Silicon/Pentacene Heterojunction	109
5.3.1	Pentacene	109
5.3.2	Device Fabrication	109
5.3.3	Current-Voltage Characteristics of Silicon/PQ/Pentacene Heterojunctions	111
5.3.4	Spectroscopy of the Silicon/PQ/Pentacene Heterojunction	114
5.3.5	Improved Silicon/PQ/Pentacene Heterojunction Solar Cell	117
5.4	Silicon/Poly(3-hexylthiophene) Heterojunction	120

5.4.1	Poly(3-hexylthiophene)	120
5.4.2	Device Fabrication	120
5.4.3	Band Modulation at the Unpassivated Si/P3HT Heterojunction	123
5.4.4	Band Alignment at the Silicon/P3HT Heterojunction	126
5.4.5	Effect of PQ Passivation	129
5.4.6	Minority Carrier Injection	130
5.4.7	Si/P3HT Heterojunction Solar Cell	138
5.5	Conclusion	153
6	Stability of Silicon/Organic Heterojunctions	154
6.1	Introduction	154
6.2	Fabrication and Methods	155
6.3	Stability of PQ-passivated Silicon Surfaces	156
6.3.1	Effect of Illumination: Light Annealing	156
6.3.2	Temporal Stability: Without Encapsulation	159
6.3.3	Temporal Stability: With Encapsulation	161
6.3.4	Possible Mechanism	166
6.4	Conclusion	168
7	Conclusions and Future Work	169
7.1	Summary of Results	169
7.2	A Case for Silicon/Organic Heterojunctions	171
7.3	Future Work	172
7.3.1	Improving Efficiency of Silicon/P3HT Heterojunction	172
7.3.2	Hole-Blocking Silicon/Organic Heterojunctions	174
7.3.3	Double-Sided Silicon/Organic Heterojunction Solar Cell	174
7.3.4	Improve Stability of Silicon/P3HT Heterojunction	175

A	Currents in Silicon Homojunction and Silicon-Organic Heterojunction Diodes	178
A.1	Introduction	178
A.2	Basic equations and nomenclature	179
A.3	Current in a n-p Homojunction Diode	182
A.4	Current in a n-p-p ⁺ Homojunction Diode	183
A.4.1	General Solution	184
A.4.2	Boundary Conditions	184
A.4.3	Current across the p/p ⁺ junction	185
A.4.4	Final Expressions	188
A.4.5	Interpretation	189
A.5	Current in the n-p-organic Heterojunction Diode	191
A.5.1	The Silicon/Organic Heterojunction	191
A.5.2	Boundary Conditions	191
A.5.3	Current Across the Si/Organic Heterojunction	192
A.5.4	Final expressions	195
A.5.5	Interpretation	196
A.6	Current in the n-Silicon/Metal Schottky Diode	199
B	Generalized Quasi-Steady-State Lifetime Measurement	203
B.1	Introduction	203
B.2	Basics	203
B.3	Relation between τ_{eff} and SRV	205
B.4	Quasi Steady-State Photoconductance Decay: Analysis	206
B.4.1	Need for Simulations	207
B.4.2	Generation Rate Profile	208
B.4.3	Data Plots and Extracted Parameters	208

C Control Metal-Oxide-Semiconductor Transistors	212
D Publications and Presentations	214
D.1 Refereed journal articles	214
D.2 Published Proceedings	215
D.3 Conference Presentations	215
D.4 Patents	216

List of Tables

1.1	Photovoltaic cost components	2
1.2	Comparison between different solar cell technologies	8
1.3	Ideality factors for different recombination mechanisms	10
2.1	Comparison between crystalline Si and amorphous organic thin-films	28
3.1	Measured recombination lifetime and surface recombination velocity .	59
3.2	The surface band-bending (ΔE_{BB}) in silicon for the three cases of Fig.3.9.	64
4.1	Different Implant conditions	89
4.2	Test for contact area effects	92
4.3	Test for Implant area effects	96
4.4	Si/organic heterojunction p-type contact parameters	100
4.5	Measured J_0 of various p-type contacts	101
5.1	Measured valence-band offset and IE at Si/organic interface	116
5.2	P3HT spin-coating recipes	121
5.3	Device parameters of n-Si/P3HT devices	128
5.4	Device parameters of n-Si/P3HT devices made on FZ wafers	136
5.5	Device parameters of n-Si/P3HT solar Cell	151
6.1	Possible degradation mechanisms in Si/organic solar cells	156
6.2	The evolution of PQ-passivated MISFET characteristics	166

B.1 Calculated QSSPCD parameters 210

List of Figures

1.1	Price verses performance trade off of different PV technologies	3
1.2	Band structure and I-V characteristics of a model solar cell	7
	(a) Band structure	7
	(b) Semilog plot	7
	(c) Linear plot	7
	(d) Power plot	7
1.3	the ASTM AM 1.5 (Global) spectrum	9
	(a) Spectral Irradiance	9
	(b) Photon Flux	9
1.4	Intuition behind relationship between J_0 and V_{OC}	11
	(a) Carrier flow in dark	11
	(b) Carrier flow under light	11
1.5	Use of back surface fields in solar cells	14
	(a) n^+ -p junction band diagram	14
	(b) n^+ -p- p^+ junction band diagram	14
	(c) n^+ -p- p^+ heterojunction band diagram	14
1.6	Structure of the PERL cell	17
1.7	The HIT solar cell	19
	(a) Structure	19
	(b) Band-structure	19

1.8	Band offset at the valence band of the HIT cell	20
2.1	Use of Si/organic heterojunctions in solar cells	27
	(a) n^+ -p- p^+ homojunction band diagram	27
	(b) n^+ -p- p^+ heterojunction band diagram	27
2.2	Band alignment in silicon heterojunctions	29
	(a) n^+ -p- p^+ heterojunction band diagram	29
	(b) n^+ -p- p^+ heterojunction band diagram	29
2.3	Surface defects	30
	(a) Silicon surface dangling bonds	30
	(b) Increased recombination	30
	(c) Fermi-level pinning	30
2.4	Effect of passivation at Si/organic interface	32
	(a) Si/organic interface without passivation	32
	(b) Si/organic interface with passivation	32
2.5	Use of silicon/organic heterojunction to block minority carriers	34
	(a) n^+ -p homojunction band diagram	34
	(b) n^+ -p- p^+ homojunction band diagram	34
	(c) n^+ -p- p^+ heterojunction band diagram	34
	(d) n^+ -p- p^+ heterojunction band diagram	34
2.6	Performance of a n^+ -p Si diode with a Si/organic heterojunction BSF	36
	(a) Electron-current component of J_0 verses conduction-band offset	36
	(b) Electron-current component of J_0 verses surface recombination velocity at Si/organic interface	36
2.7	Low-cost p-n junction alternatives	38
	(a) p-n junction band diagram	38
	(b) Si/metal Schottky junction band diagram	38
	(c) Electron-blocking Si/Organic heterojunction band diagram	38

(d)	Electron and hole-blocking Si/Organic heterojunction band diagram	38
3.1	QSSPCD measurement	50
(a)	Instrument schematic	50
(b)	Typical output waveforms	50
3.2	Effect of surface recombination on effective lifetime	52
3.3	Air stability of chemical passivation schemes	53
(a)	QSSPCD Data for p-Si	53
(b)	QSSPCD Data for n-Si	53
3.4	9,10-phenanthrenequinone (PQ)	55
3.5	Quasi-static photoconductance decay experiment data	57
(a)	Test Structures	57
(b)	QSSPCD Data for p-Si	57
(c)	QSSPCD Data for n-Si	57
(d)	Effective Lifetime of p-Si	57
(e)	Effective Lifetime of n-Si	57
3.6	Reaction between PQ and dimerized silicon (100) surface	59
3.7	C 1s XPS spectrum of PQ passivated p ⁺ -Si	61
3.8	The reaction between PQ and silicon as supported by the C 1s XPS data	62
3.9	Si 2p XPS spectrum of PQ-passivated	64
3.10	UPS & IPES of p ⁺ Si/PQ heterojunction	67
(a)	IPES of Si/PQ interface	67
(b)	UPS of Si/PQ interface	67
3.11	Band offsets at the Si/PQ Interface	68
3.12	Metal-Insulator-Semiconductor capacitor (MISCap) Results	70
(a)	MISCap Structure on p-Si	70
(b)	Small-signal capacitance at 1 MHz on p-Si	70

(c)	MISCap Structure on n-Si	70
(d)	Small-signal capacitance at 1 MHz on n-Si	70
3.13	n-channel Metal-insulator-semiconductor field-effect transistor (MIS-FET)	71
(a)	n-channel MISFET structure	71
(b)	MISFET I_{DS} - V_{DS} characteristics	71
(c)	MISFET transconductance	71
(d)	MISFET I_{DS} - V_{GS} characteristics	71
3.14	p-channel metal-insulator-semiconductor field-effect transistor (MIS-FET)	72
(a)	p-channel MISFET structure	72
(b)	MISFET I_{DS} - V_{DS} characteristics	72
(c)	MISFET transconductance	72
(d)	MISFET I_{DS} - V_{GS} characteristics	72
3.15	Extracted field-effect mobility for MISFET and MOSFET	75
(a)	MISFET Dimensions	75
(b)	Control MOSFET Dimensions	75
(c)	MISFET electron mobility	75
(d)	MOSFET electron mobility	75
(e)	MISFET hole mobility	75
(f)	MOSFET hole mobility	75
4.1	Use of silicon/organic heterojunction to block minority carriers	79
(a)	p-n junction band diagram	79
(b)	p-n junction band diagram	79
(c)	p-n junction band diagram	79
4.2	Simulations to prove the utility of a p-type silicon/organic heterojunction contact	80

(a)	Proof of concept structure: n ⁺ -p-organic diode	80
(b)	Band structure of n ⁺ -p-organic diode	80
4.3	Simulations to prove the utility of a p-type silicon/organic heterojunc- tion contact	82
(a)	Simulated electron density profile in n ⁺ -p-organic diode	82
(b)	Simulated IV characteristics of n ⁺ -p-organic diode	82
(c)	Contribution of electron and hole currents to the total current	82
(d)	Simulated and analytical electron current as a function of $S_{Si,org}$	82
4.4	The minority-carrier probe	84
(a)	Device structure	84
(b)	Band diagram	84
(c)	Simulated IV characteristics	84
4.5	The minority-carrier probe with silicon/organic heterojunction contact	85
(a)	Device structure	85
(b)	Band diagram	85
(c)	Simulated IV characteristics	85
(d)	Simulated IV characteristics at different surface recombination velocities	85
4.6	Selectivity of the minority-carrier probe design under device variations	86
(a)	As a function of implant doping	86
(b)	As a function of implant depth	86
(c)	As a function of Epi doping	86
(d)	As a function of average minority-carrier lifetime	86
4.7	Minority carrier probe	88
(a)	Simulated doping profile	88
(b)	Si/metal Structure	88
(c)	Si/metal band diagram	88

4.8	Effect of implant doping on minority-carrier probe	89
	(a) Simulated doping profile for different implants	89
	(b) IV characteristics	89
4.9	Effect of highly doped Epi layer on minority-carrier probe	91
	(a) Structure	91
	(b) Band-diagram	91
	(c) Simulated IV characteristics	91
	(d) IV characteristics	91
4.10	Effect of contact shape on minority-carrier probe	92
	(a) Top view of the structure	92
	(b) IV characteristics	92
4.11	Explanation for dependence of total current on Si/metal area	93
4.12	Effect of area scaling on minority-carrier probe	96
	(a) Top view of the structure	96
	(b) IV characteristics	96
4.13	Device Structure and band Diagrams for different p-type contacts	99
	(a) Si/metal Structure	99
	(b) Si/metal band diagram	99
	(c) Structure	99
	(d) Si/p ⁺ -Epi/metal	99
	(e) Structure	99
	(f) Si/TPD/metal	99
4.14	Effect of Si/PQ/TPD heterojunction on minority-carrier probe	100
5.1	Low-cost p-n junction alternatives	105
	(a) p-n junction band diagram	105
	(b) Si/metal Schottky junction band diagram	105
	(c) Electron-blocking Si/Organic heterojunction band diagram	105

5.2	Simulated silicon/organic heterojunction as a p-n junction alternative	106
	(a) Proof of concept structure: metal-organic-nSi diode	106
	(b) Band structure of metal-organic-nSi diode	106
	(c) Simulated IV characteristics (in dark) of metal-organic-nSi diode	106
	(d) Simulated IV characteristics (in light) of metal-organic-nSi diode	106
5.3	Simulations to explain weak dependence on surface recombination . .	107
	(a) Simulated electron density profile at the silicon/organic interface	107
	(b) Simulated conduction band diagram at the silicon/organic interface	107
5.4	Si/PQ/pentacene heterojunction	110
	(a) n-Si/PQ/pentacene test structure	110
	(b) Expected band diagram of n-Si/PQ/pentacene test structure . .	110
	(c) p-Si/PQ/pentacene test structure	110
	(d) Expected band diagram of p-Si/PQ/pentacene test structure . .	110
5.5	Si/PQ/pentacene heterojunction I-V characteristics	112
	(a) n-Si I-V characteristics in log scale	112
	(b) n-Si I-V characteristics in linear scale	112
	(c) p-Si I-V characteristics in log scale	112
	(d) p-Si I-V characteristics in linear scale	112
5.6	Effect of field on photocurrent of a n-Si/PQ/pentacene diode with a valence band offset	113
	(a) Positive bias	113
	(b) Positive bias	113
5.7	Spectroscopy of Si/PQ/pentacene heterojunction	115
	(a) Evolution of n-Si/PQ/pentacene interface	115
	(b) n-Si/PQ/pentacene band alignment	115
	(c) Evolution of p-Si/PQ/pentacene interface	115
	(d) p-Si/PQ/Pentecene band alignment	115

5.8	Measured band diagram of Si/PQ/pentacene heterojunction	116
	(a) Revised band diagram of n-Si/PQ/pentacene test structure	116
	(b) Revised band diagram of p-Si/PQ/pentacene test structure	116
5.9	Improved Si/PQ/pentacene heterojunction J-V characteristics	118
	(a) p-Si I-V characteristics in linear scale	118
	(b) n-Si I-V characteristics in log scale	118
	(c) n-Si I-V characteristics in linear scale	118
5.10	Test Structures for testing Si/P3HT heterojunction	122
	(a) Si/metal test structure	122
	(b) Si/metal band diagram	122
	(c) Si/P3HT heterojunction test structure	122
	(d) Si/P3HT heterojunction band diagram	122
5.11	Capacitance-voltage characteristics of n-Si/P3HT heterojunction	125
	(a) Raw C-V characteristics	125
	(b) $1/C^2$ -V characteristics	125
	(c) $1/C_{Si}^2$ - V_{Si} characteristics	125
	(d) Implied silicon doping	125
5.12	Effect of n-Si/P3HT heterojunction on I-V characteristics	126
	(a) On J_0	126
	(b) On V_{OC}	126
5.13	Effect of PQ on the I_V characteristic of an – Si/P3HT heterojunction	129
	(a) Test structure with PQ passivation	129
	(b) I-V characteristics of n-Si/PQ/P3HT heterojunction	129
5.14	Contribution of electron and hole current to total dark-current	131
	(a) Si/metal Schottky junction	131
	(b) Si/organic heterojunction	131

5.15	Importance of minority-carrier current in Si/P3HT heterojunction devices	131
5.16	Set up to measure storage time in Si/P3HT heterojunction devices	132
	(a) Circuit to measure storage time	132
	(b) Voltage and current waveforms	132
5.17	Measurement of storage times in Si/P3HT devices with different P3HT layer thickness	135
	(a) No P3HT	135
	(b) 2 nm of P3HT	135
	(c) 5 nm of P3HT	135
	(d) 25 nm of P3HT	135
	(e) Storage time for different P3HT thickness and forward-bias current	135
5.18	Effect of Si doping on IV characteristics of Si/organic device	136
	(a) Dark IV characteristics	136
	(b) Light IV characteristics	136
5.19	Effect of Si doping and lifetime on Si/P3HT heterojunction diodes	137
	(a) IV in dark	137
	(b) IV under 0.1 sun illumination	137
5.20	Si/P3HT heterojunction solar cell with metal grid	138
	(a) Side view	138
	(b) Top view	138
5.21	Photovoltaic response of Si/P3HT heterojunction solar cells with top metal grid	139
	(a) V_{OC}	139
	(b) I_{SC}	139
	(c) Fill factor	139
5.22	PEDOT:PSS conductivity measurements	141

(a)	Test structure for vertical resistance	141
(b)	Vertical I-V characteristics	141
5.23	PEDOT:PSS conductivity measurements	142
(a)	Test structure for lateral resistance	142
(b)	Lateral I-V characteristics	142
(c)	Lateral resistivity	142
(d)	Implied power loss	142
5.24	Losses due to lateral resistance of PEDOT:PSS	144
5.25	Photovoltaic response of Si/P3HT heterojunction solar cells with PE- DOT & metal grid	146
(a)	Structure of the heterojunction solar cell	146
(b)	V_{OC}	146
(c)	I_{SC}	146
(d)	Fill factor	146
5.26	Ohmic losses in the metal fingers	148
(a)	Schematic	148
(b)	Calculations	148
5.27	Transmission losses through organic layers	150
(a)	Transmission through PEDOT	150
(b)	Transmission through P3HT	150
(c)	Transmission through PEDOT/P3HT stack	150
5.28	Optimized heterojunction solar Cell	152
(a)	Structure	152
(b)	I-V characteristics in dark	152
(c)	I-V characteristics in light	152
6.1	“Light Annealing” of PQ-passivated p-type silicon wafers	157
(a)	Test Structure	157

(b)	Measured minority-carrier lifetime and SRV	157
6.2	Air stability of PQ-passivated silicon wafers	160
(a)	Test Structure	160
(b)	Measured minority-carrier lifetime SRV	160
6.3	Evolution of an encapsulated silicon wafer with PQ passivation	162
(a)	Test Structure	162
(b)	Measured minority-carrier lifetime	162
6.4	Stability of PQ-passivated metal-insulator-silicon capacitor	163
(a)	Device structure	163
(b)	C-V characteristics just after fabrication	163
(c)	C-V characteristics after 4 months	163
6.5	Stability of metal-insulator-semiconductor field-effect transistor (MIS-FET)	165
(a)	MISFET structure	165
(b)	Evolution of $I_{DS}-V_{GS}$ characteristics	165
(c)	MISFET transconductance after fabrication	165
(d)	MISFET transconductance after 2 months	165
6.6	Stability of metal-insulator-semiconductor field-effect transistor (MIS-FET)	166
(a)	MISFET $I_{DS}-V_{DS}$ characteristics after fabrication	166
(b)	MISFET $I_{DS}-V_{DS}$ characteristics after 2 months	166
6.7	Mechanism to explain stability of encapsulated Si/PQ interface	168
7.1	Band diagram of hole-blocking heterojunction	174
(a)	Minority-carrier blocking heterojunction	174
(b)	Majority-carrier blocking heterojunction	174
7.2	Double-sided heterojunction cell on n-Si	175

A.1	Current due to thermionic emission	181
A.2	Band diagram of the n-p-p ⁺ homojunction	183
A.3	Band diagram of a general n-p-organic heterojunction.	192
A.4	Currents in Si/metal schottky junction	199
B.1	Analysis of QSSPCD data for p-type Si	209
	(a) Oxide-coated wafer	209
	(b) Native-oxide-coated wafer	209
	(c) PQ-coated wafer	209
B.2	Analysis of QSSPCD data for n-type Si	211
	(a) Oxide-coated wafer	211
	(b) Native-oxide-coated wafer	211
	(c) PQ-coated wafer	211
C.1	Metal-oxide-semiconductor field-effect transistor (MOSFET)	213
	(a) Control n-channel MOSFET structure	213
	(b) p-channel MOSFET structure	213
	(c) n-channel MOSFET transconductance	213
	(d) p-channel MOSFET transconductance	213
	(e) n-channel MOSFET I_{DS} - V_{GS} characteristics	213
	(f) p-channel MISFET I_{DS} - V_{GS} characteristics	213

Chapter 1

Introduction

1.1 Motivation

There is an emerging need to reduce our dependence on fossil fuels and shift to renewable sources of energy. Solar photovoltaic (PV) devices, or solar cells, are a promising way to convert sunlight into electricity. However, as of 2010, solar PV accounted for just 0.03% of the total energy generation in the US [1]. The primary reason for the low market penetration is higher costs. Compared to conventional sources, solar electricity is too expensive, mostly due to the high upfront costs of manufacturing and installing solar modules.

In the solar PV market, many different technologies exist, each with a different price and performance trade off. To allow absolute comparison between the competing PV technologies, PV panels are quoted in terms of “dollar per watt-peak” (\$/W_p). This ratio takes into account that one needs fewer number of more efficient modules to generate the same amount of total power. “Watt-peak” simply refers to the fact that, solar panels are rated for power produced at the peak light intensity, even though the actual power output varies during the day.

Crystalline silicon PV is the dominant technology with 80% of the market share.

Table 1.1: Cost estimate of various components of a photovoltaic module in 2010 (without cell and module manufacturer’s margin) [2]

Component	Cost (\$/Wp)
Silicon	0.54
Raw materials (Si feedstock, saw slurry, saw wire)	0.36
Utilities, maintainance, labor	0.04
Equipment, tooling, building, cost of capital	0.06
Margin	0.08
Cell	0.26
Raw materials (eg. metallization, SiNx, dopants, chemicals)	0.18
Utilities, maintainance, labor	0.04
Equipment, tooling, building, cost of capital	0.04
Module	0.36
Raw materials (eg. Glass, EVA, metal frame, j-box)	0.26
Utilities, maintainance, labor	0.01
Equipment, tooling, building, cost of capital	0.01
Shipping	0.08
Total	1.16

Silicon cells are efficient (13-20 % average efficiencies), but they are expensive. As of 2010, average manufacturing costs of silicon-based PV modules were 1.16 \$/Wp (cell and module manufacturer margins not included) [2], not only because silicon is expensive, but also because fabrication of an efficient cell requires several high-temperature steps, complicated equipments, and expensive materials [3, 4, 5] (Table 1.1). [6].

One way to reduce cost (\$/Wp) is to compromise on efficiency and use cheaper materials: electrically inferior thin-film semiconductors instead of more expensive crystalline Si. The lower raw material costs, low-temperature processing, cheaper capital equipments, and higher throughput manufacturing allow these “thin-film” technologies to achieve substantial reductions in cost. First Solar’s CdTe and Oerlikon’s amorphous-Si technologies are prominent examples of this approach (Fig. 1.1).

Organic molecules with conjugated π -electron systems are also a class of thin-film semiconductors. In lieu of inter-atomic valence and conduction bands they have intra-molecular filled and empty energy levels, referred to as the highest-occupied-

molecular-orbital (HOMO) and lowest-unoccupied-molecular-orbital (LUMO), respectively [7]. The energy gap of organic materials is typically $\sim 2\text{-}3$ eV, which is larger than that of crystalline silicon (1.1 eV). The big advantage with organic materials is their manufacturability - organic thin-films can be deposited using low-cost high-throughput techniques, such as lamination, spray-coating or transfer printing [8]. Due to the cost advantages, many types of organic-based solar cells have been proposed in literature [9]. However efficiency of these devices is too low [6] and their reliability is very limited [10, 11].

1.2 This Work

In this thesis a hybrid approach is demonstrated, where organic materials are integrated with silicon to form a silicon/organic device that exploits the cost advantages of thin-film organic materials and superior performance of silicon [12, 13, 14].

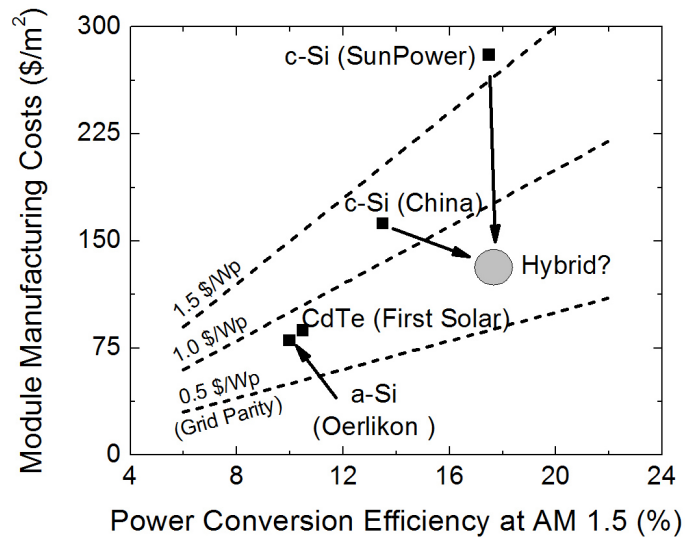


Figure 1.1: Price versus performance trade off of different PV technologies.

Like “all-organic” solar cells, hybrid devices use only low-temperature ($<150^\circ$) processing techniques and are very simple to fabricate - an organic semiconductor

is spin-coated or evaporated on top of crystalline silicon, followed by metalization. Another advantage of hybrid devices is the possibility of higher throughput - unlike dopant diffusion which is a slow step, organic inks can be deposited on silicon at extremely high speeds.

Like Si-based solar cells, light absorption and photogenerated charge separation in hybrid devices happen predominately in silicon, so losses due to poor light absorption and photogenerated carrier recombination are low. Theoretically, very high efficiencies, rivaling crystalline silicon solar cells, can be achieved in hybrid photovoltaic devices.

In addition to direct benefits discussed above, the elimination of all the high-temperature steps in solar cell fabrication has many indirect cost advantages.

1. Other than silicon melting and purification, no other energy intensive step is required, saving energy costs.
2. High throughput allows better economics of scale to reduce the fixed costs associated with each solar cell.
3. Low thermal stresses on the silicon wafers may allow use of thinner Si wafers, which reduces poly-Si (raw material) cost.
4. Capital costs are reduced because expensive high-temperature ultra-clean furnaces are replaced with less stringent and simpler equipments.
5. Many of the silicon impurities get activated during the high-temperature steps, leading to reduced minority carrier lifetimes and higher losses. Low-temperature processing may allow the use of cheaper quality silicon wafers.

In summary, “hybrid” silicon/organic photovoltaic technology is a potential candidate for low-cost *AND* efficient photovoltaics (Fig. 1.1).

1.3 Solar Cells: Basics

Structurally, solar cells are diodes that have been optimized for absorbing light and low dark-current. Like all diodes, there is a built-in electric field inside a solar cell which allows current to flow in only forward-bias (Fig. 1.2(a)). In the dark, the current-voltage characteristics are similar to that of a diode: low leakage in the reverse-bias and an exponential turn-on in the the forward bias (Fig. 1.2(b)). The current density (J) depends on the voltage across the device (V) as

$$J(V) = J_0 (e^{qV/nkT} - 1) \quad (1.1)$$

where k is the Boltzmann constant, T is the temperature, n is the ideality factor, and J_0 is the saturation current density of the diode. In the case of low-level minority carrier injection and dominance of the Shockley-Read-Hall recombination, n is unity, and J_0 is given by

$$J_0 = q \frac{D_p}{L_p} \frac{n_i^2}{N_D} + q \frac{D_n}{L_n} \frac{n_i^2}{N_A} \quad (1.2)$$

n_i is the intrinsic carrier density, N_D and N_A are the extrinsic doping concentrations in the n- and p-type regions, D_n and D_h are diffusion coefficients of electrons and holes in silicon, and L_n and L_h are the diffusion lengths of minority carriers. The equation assumes the long-base approximation is valid.

Under illumination, photons get absorbed in silicon, generating electron and hole pairs. The built-in electric field separates these charges and forces them towards opposing electrodes, causing a photocurrent (J_L) (Fig. 1.2(c)). The current voltage

characteristics in this case are given by

$$\begin{aligned}
 J(V) &= J_0 (e^{qV/nkT} - 1) - J_L \\
 P_{generated}(V) &= (J_0 (e^{qV/nkT} - 1) - J_L) V
 \end{aligned}
 \tag{1.3}$$

The generated power (P), given by the product of voltage and current (negative values represent generated power), has a global maximum, called the peak power point. To extract maximum energy from a solar cell, it should be biased near the peak power point.

The performance of solar cells is typically measured in terms of three figures of merit: the short-circuit current (J_{SC}), the open-circuit voltage (V_{OC}), and the fill-factor (FF). For the case when the series resistance (R_s) is zero, Eq.(1.3) gives

$$\begin{aligned}
 J_{SC} &= J_L \\
 V_{OC} &= \frac{nkT}{q} \ln \left(\frac{J_{SC}}{J_0} + 1 \right) \\
 FF &= \frac{P_{max}}{V_{OC} J_{SC}} \\
 \eta &= \frac{V_{OC} J_{SC} FF}{P_{in}}
 \end{aligned}
 \tag{1.4}$$

where η is the power conversion efficiency. The peak power is generated at some intermediate point between J_{SC} and V_{OC} (Fig. 1.2(d)).

1.4 Efficiency of Silicon Solar Cells

To increase the efficiency of a solar cell, at least one of the figures of merit, (J_{SC}), V_{OC} , or FF, needs to be increased. The record efficiencies published in the literature of various solar cell technologies are give in Table 1.2 [6]. To better compare the different technologies the implied J_0 of the diodes, calculated from the solar cell parameters

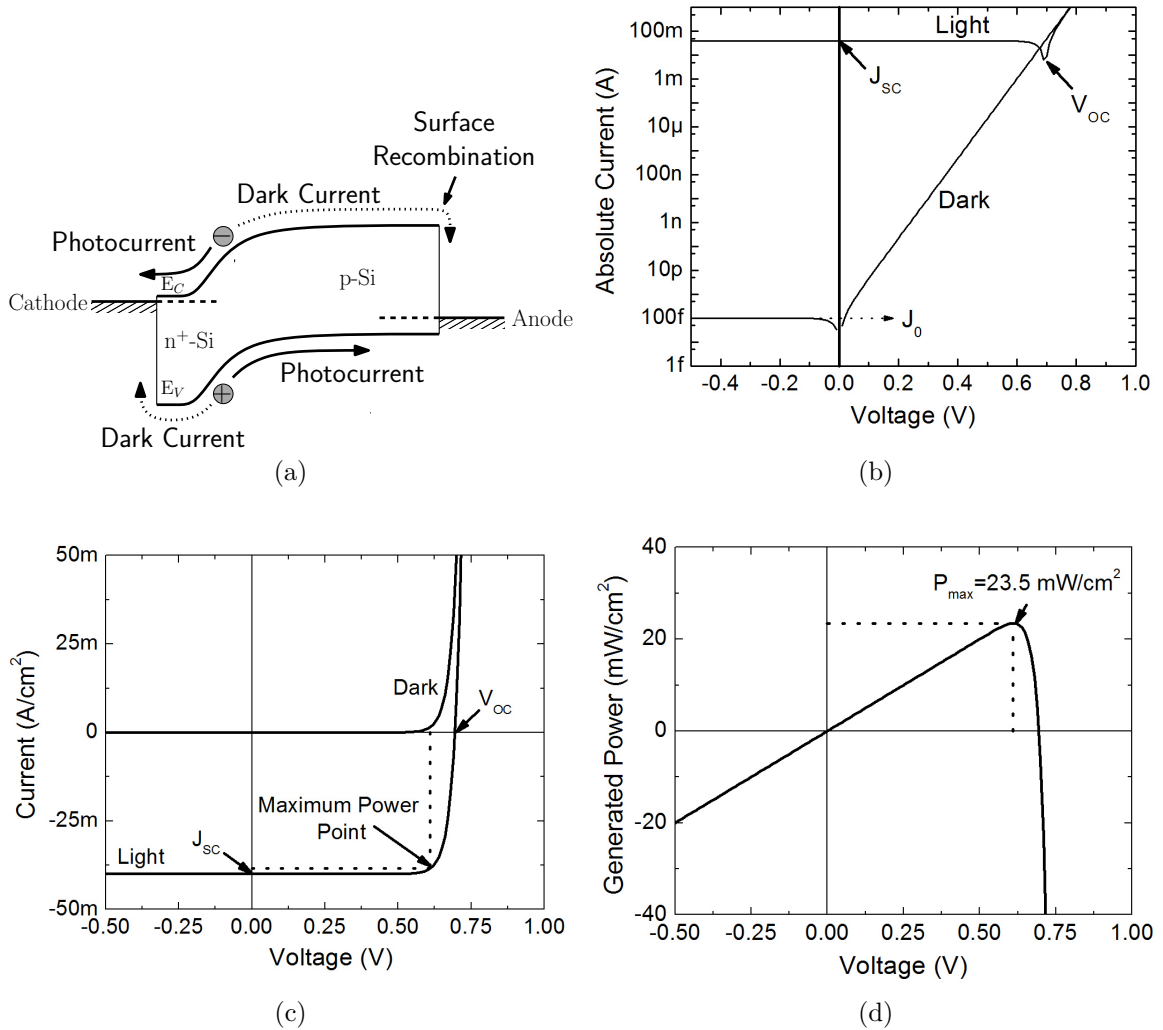


Figure 1.2: (a) The band-diagram of a model diode with J_0 of 10^{-13} A/cm², along with I-V characteristics in dark and under AM 1.5 illumination, plotted on (b) semilog and (c) linear axes. (d) The generated power as a function of voltage, showing the maximum power point.

using Eq. (1.4), is also shown.

1.4.1 Short-Circuit Current

For the simple case of constant generation across the whole depth of a solar cell, the J_{SC} is given by

$$J_{SC} = qG(L_n + L_p) \quad (1.5)$$

Table 1.2: Performance of different solar cell technologies at AM1.5 conditions [6]. Reported values of solar cell parameters: Efficiency (η), V_{OC} , J_{SC} and FF. Implied value of J_0 was calculated using Eq. (1.4).

Cell Type	η (%)	V_{OC} (V)	J_{SC} (mA/cm ²)	FF (%)	Area (cm ²)	$J_0^{(a)}$ (A/cm ²)
Single-crystalline Si	25.0±0.5	0.706	42.7	82.8	4.00	6.9×10 ⁻¹⁴
HIT (c-Si/a-Si)	23.0±0.6	0.729	39.6	80.0	155.1	2.6×10 ⁻¹⁴
Multi-crystalline Si	20.4±0.5	0.664	38.0	80.9	1.002	3.1×10 ⁻¹³
Thin film transfer Si	16.7±0.4	0.645	33.0	78.2	4.017	5.6×10 ⁻¹³
Amorphous Si	10.1±0.3	0.886	16.75	67.0	1.036	2.6×10 ⁻¹⁷ ^(b)
Single-crystalline GaAs	27.6±0.8	1.107	29.6	84.1	0.9989	9.6×10 ⁻²¹
CIGS	19.6±0.6	0.713	34.8	79.2	0.996	4.3×10 ⁻¹⁴
CdTe	16.7±0.5	0.845	26.1	75.5	1.038	2.0×10 ⁻¹⁶
Organic	8.3±0.3	0.816	14.46	70.2	1.031	3.4×10 ⁻¹⁶ ^(b)

^(a)Extracted from given parameters using Eq. (1.4)

^(b)Due to low FF, extracted value is inaccurate.

where, G is the generation rate due to illumination and L_p & L_n are the hole and electron diffusion lengths, respectively. The relation assumes that the depletion width in both n and p regions is much less than the diffusion lengths, L_p & L_n . The relation also neglects the effect of surface recombination. For a solar cell in which the diffusion lengths are longer than the wafer thickness ($L_n, L_p > W$), the diffusion term drops off and the short-circuit current depends only on the photon-flux of the incident light.

Solar insolation spectrum closely matches the broadband spectrum of a 5777 °K blackbody [15], but due to atmospheric absorption the actual spectrum reaching earth is strongly confined between the far infrared and near ultraviolet. Solar cell efficiencies are normally quoted against the ASTM AM 1.5 (Global) standard illumination (Fig. 1.3) [16]. The incident power at AM 1.5 illumination is 100 mW/cm² (Fig. 1.3(a)). By dividing the spectral irradiance (I_λ) with photon energy ($\frac{hc}{\lambda}$), the spectral photon flux (Φ_λ) can be extracted (Fig. 1.3(b)).

A semiconductor with a given bandgap (E_G) strongly absorbs photons with energies greater or equal to E_G . Some phonon-mediated absorption does occur at lower

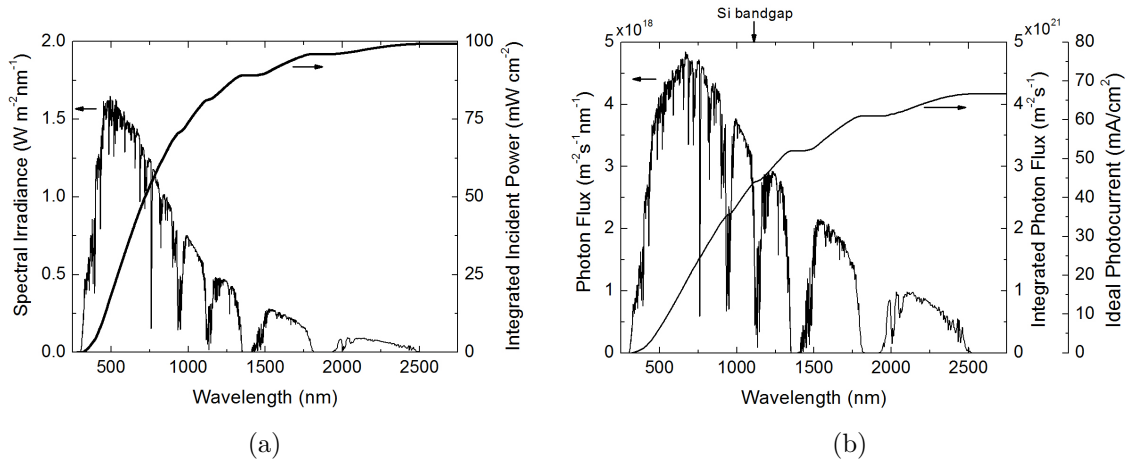


Figure 1.3: (a) The spectral irradiance and integrated power density of the 100 mW/cm² AM 1.5 (Global) standard. (b) Incident photon flux as a function of wavelength. The maximum photocurrent densities at each wavelength are also shown.

energies but the absorption lengths are so long (~ 1 mm in silicon) that not many carriers are generated by this process in a 200-500 μm thick silicon wafer. Assuming each photon generates an electron-hole pair, i.e. an internal quantum efficiency of 1, the maximum possible photocurrent at a given wavelength cutoff can be calculated (Fig. 1.3(b)). For silicon, whose bandgap is 1.12 eV, only wavelengths below 1110 nm are absorbed and the maximum photocurrent is 43.8 mA/cm² [17]. State of the art crystalline solar cells reach very close to the maximum value ($J_{SC} > 42$ mA/cm²) by clever use of light-trapping structures and anti-reflection coatings [18].

1.4.2 Fill-Factor

Fill factors decrease with increase in the internal series resistance. Usually, the top metal grid covers only 5-10% of the top surface, so photogenerated carriers need to travel large lateral distances before they are collected at the metal contact. If the conductivity of the top semiconductor layer is not high enough, the resulting ohmic losses reduce the fill-factor [19].

Fill factors also reduce if the ideality factor (n) of the solar cells increases. The

Table 1.3: Ideality factors (n) resulting from different recombination mechanisms that may have been observed in solar cells.

Recombination Type	n	Description
SRH in quasi-neutral region (low-level injection)	1	Minority carrier limited.
Band to band (low-level injection)	1	Minority carrier limited.
SRH in quasi-neutral region (high-level injection)	2	Both carriers needed.
Band to band (high-level injection)	2	Both carriers needed.
SRH in depletion region	2	Both carriers needed.
Auger	$\frac{2}{3}$	Two majority and one minority carriers needed.

ideal diode-characteristics (Eq. (1.1)) assume that current flows only due to low-level minority-carrier injection (into quasi-neutral regions) and carrier recombination only via the Shockley-Read-Hall (SRH) mechanism [20]. In a practical cell, current can be caused by several other mechanisms (Table 1.3), e.g high-level minority carrier injection ($n=2$) [21], Auger recombination ($n=\frac{2}{3}$) [22], recombination in the depletion region of the diode ($n=2$) [23, 24]. Non-uniformity in the doped layers is also reported to cause higher ideality factors [25]. Current contribution of these non-ideal processes have different voltage dependence than the ideal case of Eq. (1.1) and consequently ideality factors of practical devices deviate from unity.

Both increased ideality and higher fill factors can be a big issue in thin-film devices, because the mobilities and diffusion lengths of carriers in amorphous materials are usually poor. However, in the case of high-quality crystalline silicon solar cells fill-factors that are very close to the theoretical maximum ($>80\%$) are easily obtained.

1.4.3 Open-Circuit Voltage

Since J_{SC} and fill-factor are already near the theoretical maximum in practical silicon solar cells, the only parameter available for further improvement is V_{OC} . Improvements in V_{OC} require a reduction in J_0 (according to Eq. (1.4)). To understand the intuitive reasoning behind the relationship between J_0 and V_{OC} , we need to first un-

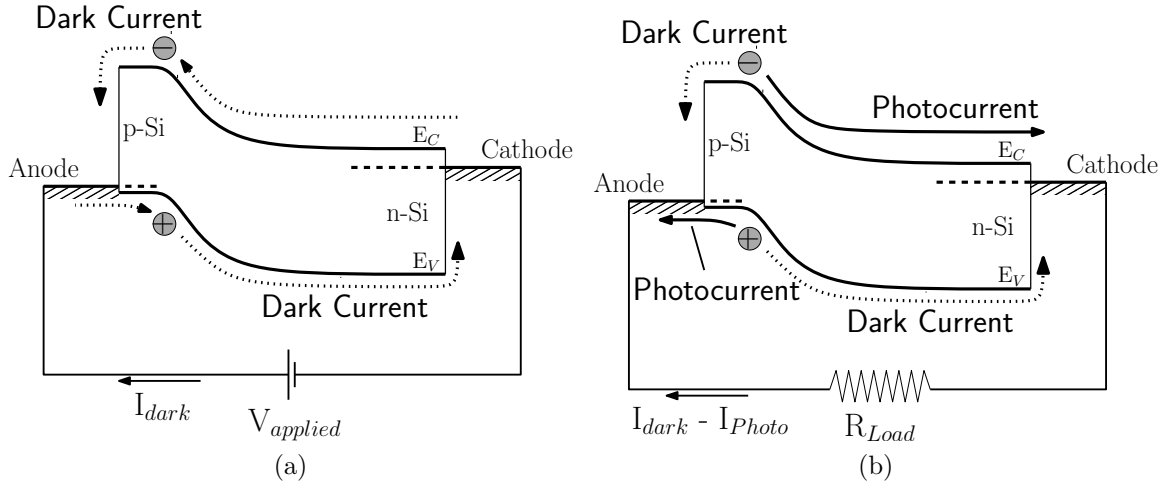


Figure 1.4: The directions of electron and hole flow in a forward-biased p-n junction diode. The dashed line represent the dark-current, while solid lines represent photocurrent. (a) In dark, current due to minority carrier recombination flows from anode to cathode. (b) Under illumination, the photogenerated current (I_{Photo}) flows from cathode to anode, but some of it lost due to dark-current.

derstand the physical process what J_0 represents. Consider a p-n junction silicon diode (Fig. 1.4).

Theoretically, J_0 of the device depends on the minority carrier diffusion lengths and bulk doping as per Eq. (1.2) [20]. At equilibrium, the diffusion current (due to carrier density gradient) equals the drift current (due to the built-in field), and the net current is zero. When a forward-bias is externally applied across the p-n junction ($V_{applied}$) the built-in field is reduced, upsetting the drift-diffusion balance. The more dominant diffusion current injects minority-carriers across the junction into the quasi-neutral region, where they recombine. Holes are injected from p-Si to n-Si, electrons are injected from n-Si to p-Si, resulting in a positive current flow from anode to cathode (dotted lines of Fig. 1.4). The higher the injected minority-carrier current, the higher J_0 . So J_0 is simply a measure of minority carrier recombination in the diodes.

Under illumination, excess carriers are created in the quasi-neutral regions of silicon due to photogeneration. The built-in field tries to re-establish equilibrium

by flushing out the photogenerated carriers, electrons towards the cathode and holes towards the anode (solid lines of Fig. 1.4b), thereby causing a photocurrent, in the direction opposite to the minority carrier current and a positive photovoltage (exact values depend on the load resistance). However, due to a positive photovoltage and resulting reduction in built-in field, some of the minority carriers go the “wrong way”, i.e. they are injected across the junction and lost to recombination (dotted lines of Fig. 1.4b). The amount of current lost to recombination is precisely the value of the dark-current at that voltage. By decreasing J_0 , we are reducing the amount of carriers lost to recombination, and so a lower J_0 should lead to a more efficient solar cell (higher V_{OC}).

1.5 Methods to Reduce J_0 : Back Surface Fields

1.5.1 Reducing Bulk Recombination

One way to reduce the recombination losses is to increase the minority carrier diffusion lengths in bulk silicon. This is usually achieved by replacing silicon wafers grown by the Czochralski (CZ) process with wafers grown by the Float-zone (FZ) process. Compared to CZ wafers, FZ wafers are known to have long minority carrier recombination lifetime; a <1 ms for CZ compared [26] to ~ 10 ms for FZ [27], partially due to the lower oxygen and carbon content [28]. The world-record 25 % solar cell [18] was fabricated on FZ-silicon. However, this technology has limited commercial potential because FZ wafers are many times more expensive than CZ wafers. Other options, such as magnetic CZ [28], have been demonstrated, which try to find a middle ground between quality and price of silicon wafers.

Another way to reduce minority carrier injection is to increase the doping of the silicon substrate, since J_0 is inversely proportional to substrate doping (N_D) as per (1.2). However, minority carrier lifetimes are known to degrade (i.e. diffusion lengths

L_n and L_p decrease) with increasing doping concentration [29], so there is an upper limit to which doping can be increased. Silicon solar cells typically use 1 Ωcm p-Si wafers with $\sim 100 \mu\text{s}$ lifetime [28].

1.5.2 Reducing Surface Recombination

The cost of poly-silicon, the source material for the growth of crystalline silicon, is a big component of total cost (Table 1.1), so manufacturers prefer thinner silicon wafers. At present the industry standard is a 150-200 μm thick silicon wafer with bulk minority carrier lifetimes of $>100 \mu\text{s}$ [30]. Since the minority carrier diffusion lengths in these devices ($\sim 500 \mu\text{m}$) are longer than the wafer thickness, most of the recombination occurs not in the bulk, but at the surfaces (Fig. 1.5(a)).

Use of Homojunction Surface Fields

To reduce surface recombination, solar cells use a variety of structures, which in literature are collectively referred to as the front/back surface fields (BSF and FSF). The structure used to create these surface fields, typically consist of a combination of dielectric layers (silicon oxide and silicon nitride), floating p-n junctions, and doped high-low junctions (p/p⁺ or n/n⁺) [31].

The surface recombination is particularly acute at the metalized silicon surface because the Si/metal interface is known for very high surface recombination velocities (SRV) [32, 31]. Under certain assumptions discussed in Appendix A,

$$SRV_{metal} = \frac{A^*T^2}{qN_C} \quad (1.6)$$

where, A^* is the effective Richardson constant, T is the temperature, N_C is the conduction band density of states, and q is the electronic charge. At 300 °K, $SRV_{metal} > 10^6 \text{ cm/s}$. The most common method to reduce Si/metal recombination is through

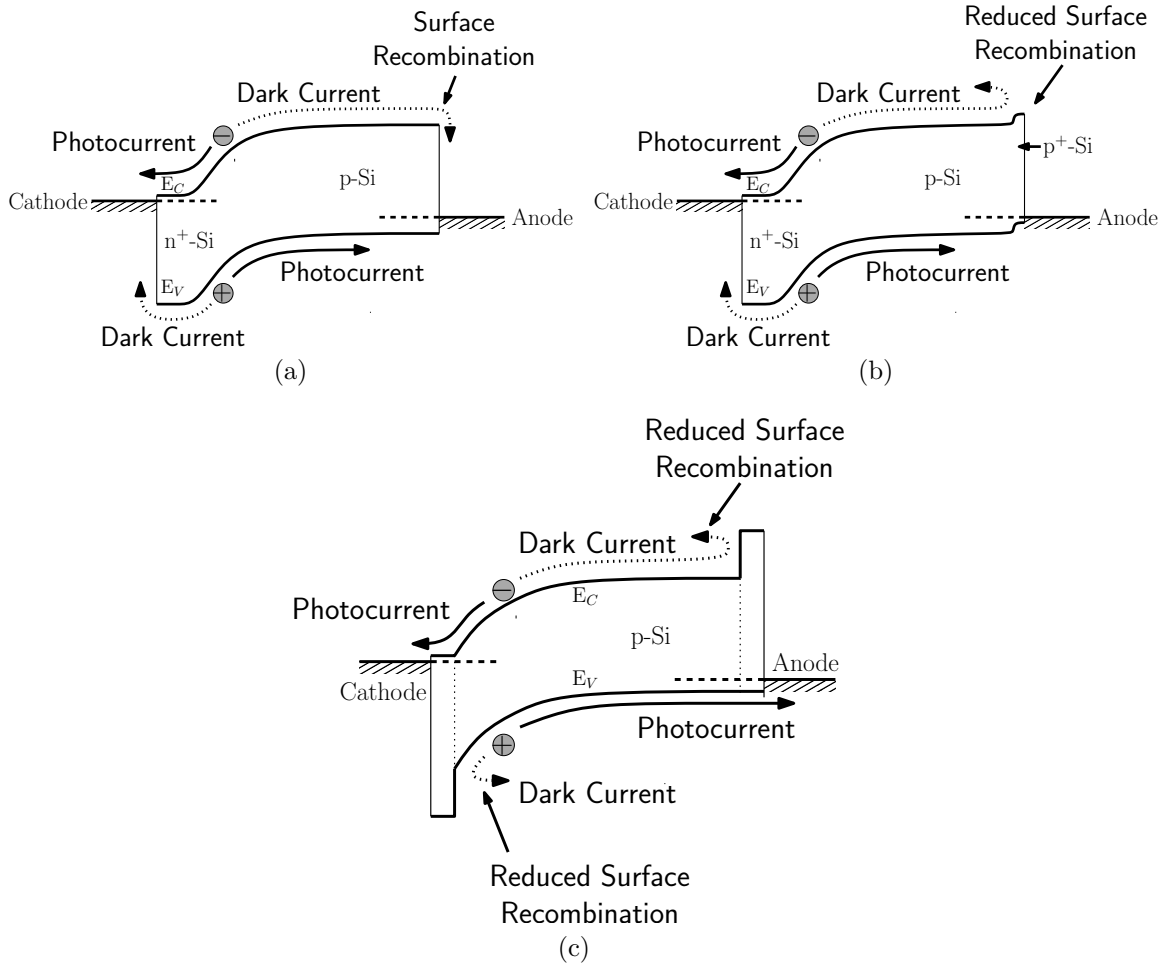


Figure 1.5: (a) Band Diagram of solar cell in which recombination at the metal contact dominates. The solid lines are desired direction of photogenerated carrier flow and the dashed line represents dark current, or equivalently the loss mechanism. (b) Effect of a p/p^+ back surface field in reducing the electron recombination at the anode. (c) Effect of a well designed wide-bandgap silicon heterojunction that reduces the electron recombination at the anode using the barrier induced by the offset in the conduction band.

a high-low junction, which for solar cells made on p-type Si involves the addition of a highly doped p^+ layer underneath the Si/metal interface. The resulting p/p^+ junction induces an electric field at the silicon surface which repels the electron away from the junction, thereby reducing surface recombination (Fig. 1.5(b)).

While the silicon homojunction cells have good performance, they do suffer from two disadvantages a) the energy barrier associated with high/low junctions is only \sim

0.2 eV, which limits the performance of the minority-carrier blocking back-surface-field and b) the fabrication of diffused junctions requires high-temperature steps and specialized equipment.

Use of Heterojunction Surface Fields

One possible way to achieve larger surface-fields and reduce fabrication costs is to replace diffused homojunctions with wide-bandgap heterojunctions on both sides of silicon [33] (Fig. 1.5c). In such a structure the heterojunction at the anode blocks minority-carriers (electrons) and a different heterojunction at the cathode blocks the majority carriers (holes). Together, the two heterojunctions replace the back surface field and p-n junction, respectively, of the conventional silicon structure.

The wide-bandgap material at each of the heterojunctions has to satisfy certain band-alignment criteria. On the anode side, the proposed heterojunction requires a wide bandgap semiconductor with:

- (a) a conduction-band edge that is much higher than conduction band edge of silicon, i.e. there should be a large conduction band offset to block electrons and
- (b) a valence-band edge that is aligned with valence band edge of silicon, i.e. there should almost no valence band offset, so that the photogenerated holes are easily collected at the anode.

For the cathode the conditions are reversed, i.e. the heterojunction should block holes but let electrons go through.

Furthermore, the metal work-function at the two electrodes should also satisfy certain requirements. To insure that there is a built-in electric field at zero-bias, to separate photogenerated carriers, the work function of the anode metal should be high (>4.9 eV) while the work-function of the cathode metal should be low (<4.2

eV).

1.6 Previous Work

Several review articles, provide a good in-depth review of all present day silicon-based solar cell technologies [34, 35]. In this section, two representative examples are discussed, to illustrate some important solar cell concepts that are relevant to this thesis.

1.6.1 PERL Cell: Representative n^+ - p - p^+ Homojunction Solar Cell

Developed at the University of New South Wales, the passivated emitter and rear locally diffused (PERL) cell is a standard n^+ - p - p^+ homojunction structure used to fabricate 24% efficient solar cells [36, 18, 28, 35]. The salient features that contribute to its performance are:

- The substrate is 400 μm thick p-type FZ crystalline silicon wafer.
- The silicon surface is textured with inverted pyramids to reduce light reflection and increase “light-trapping” [37]. The longer wavelength “red” photons have long absorption lengths (~ 1 cm), so in a 400 μm thick cell, they reflect multiple times inside the cell before getting absorbed. The textured surface reduces the chance of them escaping from the top surface, hence the term “light-trapping”. The improved light absorption increases the J_{SC} .
- The top surface is covered with a thin layer of oxide (250 Å) and a double layer antireflection coating (ZnS and MgF_2). The oxide passivates the top surface and reduces recombination of carriers generated near the top surface. Oxide layers is usually grown in TCA (1,1,1-trichloroethane) ambient because it

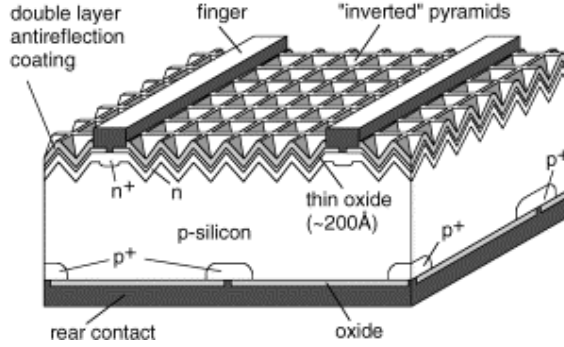


Figure 1.6: Structure of a “Passivated emitter and rear locally diffused” (PERL) solar cell [35].

helps maintain high minority-carrier lifetimes during processing and improves the quality of the passivating oxide. Reduced recombination leads to higher V_{OC} . The antireflection coating, reduces the reflection of the shorter wavelength “blue” photons from the top surface, thereby increasing J_{SC} .

- A blanket moderately-doped ($\approx 4 \times 10^{18} \text{ cm}^{-3}$) n-type layer that is used to separate photogenerated carriers and blocks holes. Highly-doped n^+ -layers suffer from several problems, such as bandgap narrowing, degeneracy, and Auger recombination, all of which degrade the solar cell performance [38]. The effect of this “dead layer” is most acute for blue photons. By reducing the n-doping the PERL structure delivers a higher J_{SC} than cells with highly-doped n-layers. In a typical cell n-layers are made by POCl_3 diffusion.
- Locally diffused highly-doped n^+ layer (also called the “emitter” layer). The highly-doped layers not only forms an effective n^+ -p junction to separate the photogenerated carriers but also prevents recombination of holes at the top Si/metal interface, thereby increasing the V_{OC} .
- Dielectrically enhanced metallic rear Al reflector, reflects the red photons back into the silicon [39]. This increases the efficiency of the light trapping and increases J_{SC} .

- Locally diffused highly-doped p^+ as the back surface field (BSF). The p/p^+ junction at the back served to reduce recombination of electrons, thereby increasing V_{OC} [40].
- Thermal-oxide-passivated back surface. Even with a p^+ BSF, the Si/metal interface at the back surface is a major cause of surface recombination. By confining the area of the Si/metal interface to less than 5-10 % of the total back area and passivating the rest with high-quality oxide [41], both J_{SC} and V_{OC} are increased [40]. The p-layers can be made either by alloying Al with silicon above their eutectic temperature ($>577^\circ\text{C}$) [42], or by diffusing boron [40]. While the performance is superior in the latter, cost and throughput consideration make the Al BSF popular in commercial solar cells.

1.6.2 HIT Cell: Representative p^+ - n - n^+ Heterojunction Solar Cell

Developed by Sanyo, “Heterojunction with intrinsic thinlayer” (HIT) solar cell implements the idea of wide-bandgap heterojunction, using hydrogenated amorphous silicon (aSi, bandgap of 1.7 eV for n-type/intrinsic and 1.6 eV for p-type aSi [43]) as the wide-bandgap material [44, 45] to block both electrons and holes. In terms of traditional silicon solar cell language, heterojunctions are used for both charge separation and back-surface field (Fig. 1.7). Some of the salient features of HIT structure are:

- At the interface between aSi and cSi, a very thin layer of intrinsic aSi is grown at both the heterojunctions. Surprisingly this i-aSi layer is extremely good at satisfying the previously unsatisfied valencies of the crystalline silicon surface, thereby passivating the silicon surface (SRV <50 cm/s [31]). Consequently solar cells with record open-circuit voltages (0.729 V) have been demonstrated

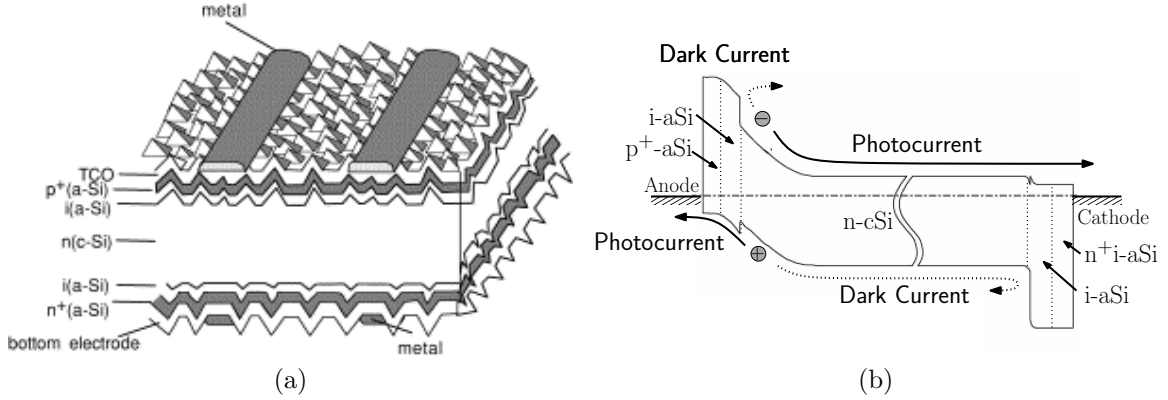


Figure 1.7: (a) Structure of a “Heterojunction with intrinsic thinlayer” (HIT) solar cell. (a) The ideal band alignment required for efficient operation [43].

[45]. Interestingly, the passivation does not work if the aSi layers are doped! It is believed that the deterioration is due to the interface states caused by the doping materials which attach to the c-Si surface during the deposition process [43].

- The top and bottom electrodes have blanket coating of sputtered ITO. Due to the high resistivity (low carrier mobility) of the even heavily-doped aSi layers, transparent conducting layers are needed on the front and back of the of the structure to allow lateral carrier transport to the metal contacts. The advantage of the approach is that even the backside of module can generate power, by absorbing the light scattered from the surroundings. The disadvantage are: high costs, conductivity losses, and transmission losses of ITO. The losses in ITO force a trade off between J_{SC} and fill-factors [46].
- The approach uses n-type phosphorus doped wafers, which is almost unique within the industry. One advantage of this approach is that, unlike cells made on p-Si, cell made on n-Si do not suffer from boron-oxygen defects [47, 48] and there appear to be no corresponding problems with phosphorus-oxygen defects. Secondly, n-Si wafers have fundamentally higher lifetimes than p-Si wafers, arguable due to lower recombination activity of metal and non-metallic

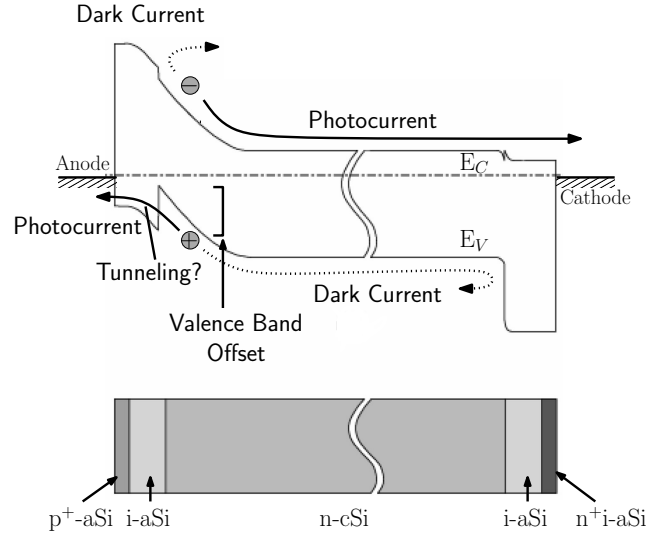


Figure 1.8: Estimated band structure for HIT cell based on published values of aSi electron affinity, showing the valence band offset that may block photogenerated holes at the anode-side heterojunction [43].

impurities [49, 50, 51].

- Processing temperatures after wafer formation are similar to those typical of amorphous silicon solar cell processing (~ 200 °C), much lower than those for normal crystalline silicon.
- Published values of aSi electron affinity suggest that there is a valence band offset between p-aSi/n-cSi [43] (Fig. 1.8). Theoretically, such an offset is expected to limit collection of photogenerated holes at the anode and reduce J_{SC} [52]. In practical HIT cells, no such effect has been reported, arguably because the holes are able to tunnel through the thin p^+ layer [43].

1.7 Thesis Outline

In this work, hybrid silicon/organic heterojunctions (SOH) are investigated for photovoltaic applications. The key contribution is identification and solution of two critical issues that have limited performance in previous devices - unpassivated midgap de-

fects at the silicon surface and band-alignment at silicon/organic interfaces. A novel organic-based passivation scheme for Si (100) surfaces has been developed that reduces silicon surface defect density without the use of any high temperature steps. Two different silicon/organic heterojunctions have been developed, one to block minority carriers from recombining at the Si/metal contacts and another to block majority carriers. These heterojunctions could be used in crystalline silicon photovoltaics as a replacement for diffused p/p⁺ and p-n junctions, thereby enabling solar cells that are fabricated at low-temperature and at low-cost, but deliver high performance.

In chapter 2, the silicon/organic heterojunctions are discussed in detail. The major challenge of such an approach - defects at the Si/organic interface - is identified and present state of the art solutions are discussed. To fully replace all high-temperature steps that are used in the fabrication of silicon solar cells, two different types of heterojunctions are required - one to replace the majority-carrier blocking p-n junctions and second to replace the minority-carrier blocking back surface field. Closed-form expressions for both types of heterojunctions are presented which highlights both the advantages and the technical challenges of the heterojunction-based approach.

In chapter 3, a solution to the fundamental problem of integrating amorphous organic onto crystalline silicon surfaces is presented. The organic small molecule, 9,10-Phenanthrenequinone (PQ), functions as a novel passivating layer, that can be deposited as an intermediate layer between the organic and silicon, to reduce the interface defect density at Si/organic heterojunctions. Minority carrier recombination lifetime measurements, X-ray spectroscopy (XPS), and field effect device characteristics are used to establish passivation quality of PQ. To better understand the impact of PQ on current transport, ultraviolet photoemission spectroscopy (UPS) and inverse photoemission spectroscopy (IPES) were used to measure band-alignment at the n and p-type silicon/PQ interfaces. The work described in this chapter was the subject of two publications [13, 14].

In chapter 4, a minority-carrier blocking silicon/organic heterojunction is presented. First a need to fabricate a special device that can be used to probe changes in minority carrier currents is identified. Next detailed simulations are used to design such a structure - called the “minority-carrier probe”. The fabricated minority carrier probe is tested and shown to function in the intended way. Using the minority carrier probe, a Si/organic heterojunction that can lower the electron current by a factor of two is demonstrated. The work described in this chapter was the subject of one paper published in a conference proceedings [12].

In chapter 5, two majority-carrier blocking silicon/organic heterojunctions are presented. The low temperature processable heterojunction can be used to replace the conventional p-n junction. Simulations and device current-voltage characteristics are used to identify the band-alignment criteria that the organic layer need to satisfy. It is shown that compared to a Si/metal device, the majority carrier currents in Si/organic/metal device are several orders of magnitude lower. Using theory, simulations and actual device measurements it is shown that further improvements in these devices require reduction of minority carrier currents. By optimizing the top electrode and silicon substrate doping, a 10% efficient crystalline silicon hybrid solar cell is demonstrated. The work described in this chapter was the subject of two papers currently under peer-review.

In chapter 6, some preliminary studies to probe the stability of the Si/organic interfaces are presented. The quality of PQ-passivation is found to be a strong function of light exposure. Exposure to UV light from a mercury lamp in the right dosages, was found to drastically decreases the surface recombination velocity. The temporal stability of PQ-passivated surfaces is also presented. Without any encapsulation, PQ-passivated silicon surfaces are found to be stable for at least 24 hours. However the stability increases to months with the even the most rudimentary encapsulation. A hypothesis explaining the light and encapsulation sensitivity of PQ-passivated surface

is presented.

In chapter 7, a summary of all the results and some ideas for future work are presented. The two heterojunctions presented in this thesis block only electrons. A similar heterojunction needs to be developed for holes, with the ultimate goal of integrating both the majority and minority-carrier blocking heterojunctions into the same device for $>20\%$ efficient solar cells. A parallel research problem could tackle the issue of stability. Present generation devices degrade within hours or months, but to really compete with conventional silicon technologies, lifetimes in excess of 20 years need to be demonstrated.

Chapter 2

Silicon/Organic Heterojunctions for Photovoltaics

2.1 Introduction

The goal of this thesis is to investigate if organic semiconductors can be used to make wide-bandgap heterojunctions on silicon. There is considerable interest in such organic/silicon devices [53, 54] because hybrid devices can exploit the advantageous properties of both classes of materials - the potential low-cost and synthetic variety of organic semiconductors with technological maturity of silicon. Using hybrid heterojunctions many novel devices have been proposed in the literature, e.g. gas sensors [55] and bio-compatible sensors [56].

Heterojunction devices are also very useful for photovoltaic applications because:

1. Theoretically the devices can be very efficient - the wide-bandgap heterojunction made by a wider-bandgap organic and silicon might lead to HIT-like solar cells with a V_{OC} that is higher than for homojunction solar cells.
2. Device are expected to be low-cost - organics can be quickly and easily deposited on silicon using potentially cheap processes such as spin-coating, spray-coating,

etc.

3. Formation of such “straddling gap” (type I) heterojunctions on silicon using inorganic semiconductors is a difficult problem [44, 57], but organic semiconductors can be easily layered on top of silicon using low-cost solution-based manufacturing.
4. Finally, organic semiconductors offer a large design space to tailor the physical and electrical properties of thin films by manipulating the chemical structure [58], making the task of designing and fabricating silicon/organic heterojunctions considerably simpler. For example, unlike HIT cells which are stuck with an undesirable valence-band offset (Chapter 1), the organic heterojunctions might be designed with a zero valence-band offset by fine-tuning the HOMO/LUMO levels of the organic semiconductor.

Despite the advantages and several previous attempts [59, 60, 61, 62, 63], the Si/organic heterojunctions have not been commercially relevant because the power conversion efficiencies achieved so far have been very low (<2-5%). The theoretical reasons for poor performance and device design to overcome these problems are the subject of this chapter.

In this chapter, first the band-alignment criteria of SOH cells will be discussed. Next two issues that are critical for silicon/organic heterojunctions will be identified: band-alignment (Section. 2.3.1) and interface defects (Section. 2.3.2). Finally design of two silicon/organic heterojunctions will be presented, each serving an important function with regard to solar cells. The first heterojunction blocks minority carriers from recombining at the p-type silicon/metal contact, increasing the open-circuit voltage, while the second blocks majority carriers from recombining at the silicon/metal contact and separates photogenerated carriers, giving rise to a photocurrent. Theoretical calculations reveal that under certain conditions, performance

of these heterojunction solar cells can exceed performance of the homojunction equivalents.

2.2 Fundamental Band Requirements of Silicon/Organic Wide-Bandgap Heterojunctions

While light is easily absorbed in crystalline silicon, efficient extraction of the photo-generated electrons and holes typically requires fabrication of diffused n-p and p-p⁺ junctions [64, 18]. In cells fabricated on p-type silicon, the two junctions serve two different functions:

- (a) The p-p⁺ low-high junction blocks minority carriers (electrons) from recombining at the anode (dotted red line in Fig. 2.5(b)).
- (b) The n⁺-p junction blocks the majority carriers (holes) from flowing to the cathode and creates the “built-in” electric field, that separates the photogenerated carriers and causes a photocurrent (solid lines in Fig. 2.5(b)).

The resulting lower dark-currents lead to a lower J_0 and high V_{OC} as per Eq. (1.4). The J_0 of well engineered n⁺-p-p⁺ junctions can be lower than 10^{-13} A/cm², which allows these cells to achieve very high power conversion efficiencies (>20%) [64, 18].

Theoretically, wide-bandgap heterojunctions are even better at reducing surface recombination due to the higher surface fields. Consequently, higher open-circuit voltages can be achieved in heterojunctions [33], e.g. HIT cells own the record for V_{OC} in silicon devices (Section 1.6.2) [44, 45]. Unfortunately there is no known wide-bandgap crystalline semiconductor that can be epitaxially deposited on crystalline silicon. Among the amorphous materials, organic semiconductors have energy gaps that are larger than 1.12 eV, so they can be expected to form wide-bandgap heterojunction with silicon.

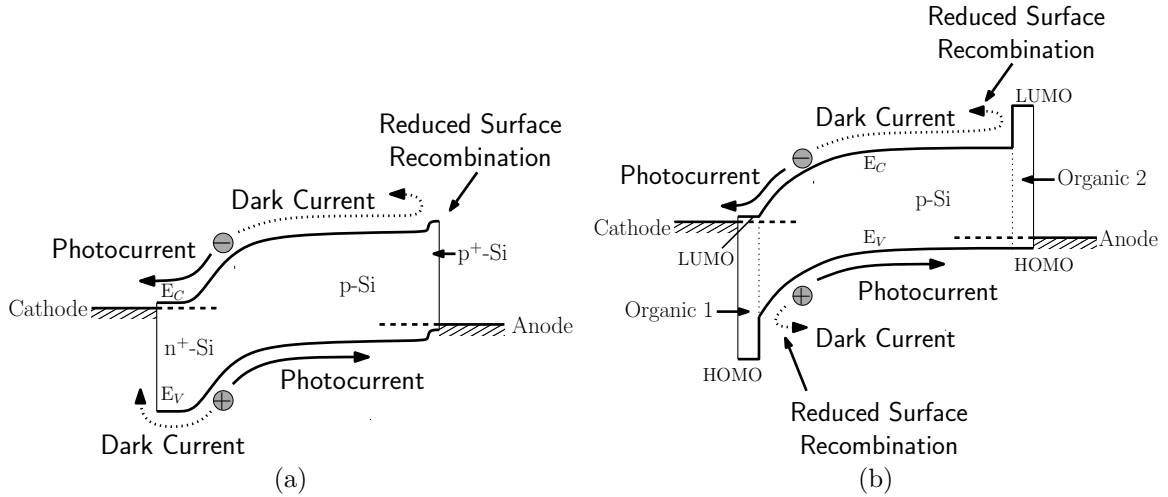


Figure 2.1: (a) The conventional n^+p-p^+ solar cell. (b) Effect of a well designed wide-bandgap silicon heterojunction that performs the same function. The solid lines are desired direction of photogenerated carrier flow and the dashed line represents dark current, or equivalently the loss mechanism.

As explained in Section 1.5 Fig. 1.5, to replace both the diffused homojunctions in crystalline Si solar cells, two different heterojunctions are needed (Fig. 2.1(b)). The heterojunction that replaces the back-surface field, requires a Si/organic interface that blocks electrons from recombining at the the anode but allows photogenerated holes to flow to the anode. The heterojunction that replaces the n-p junction requires a Si/organic interface that blocks the holes from recombining at the cathode but allows photogenerated electrons to flow to the cathode. In the next few sections both types of heterojunctions are discussed in more detail.

Finally a two important clarifications. First, the organic layers in the silicon/organic heterojunction devices of Fig 2.1 are very thin (10nm), so our intuition suggests that most of the light absorption should occur in silicon and not in the organic layer. Second, separation of photogenerated carriers also must happen in silicon because of the electric field in silicon. This is very unlike the “all-organic” solar cells, where both absorption and charge separation happen in silicon. In SOH devices, the organic layers are used only to engineer the band gaps and block carriers.

Table 2.1: Comparison between electrical properties crystalline silicon (cSi) and amorphous organic thin-film semiconductors, highlighting the problem with integrating them together.

Property	Crystalline Si	Organics
Chemical		
Atomic/molecular arrangement	Crystalline	Amorphous
Bonding	Interatomic covalent	Intermolecular Van der Walls
Filled energy level	Valence band	HOMO
Empty energy level	Conduction band	LUMO
Electrical		
Bandgap	1.12 eV	2-3 eV
Bulk mobility	100-1400 cm ² /V·s	<10 ⁻³ cm ² /V·s
Reliability	>20 years	only ~ 1 year.
Fabrication		
Deposition	Epitaxial	Thermal evaporation, solution casting, etc
Temperature	500-1000 °C	<200 °C
Potential cost	High	Low

0

2.3 Silicon/Organic Interface: Issues and Solutions

Crystalline silicon and amorphous organic thin-films are inherently dissimilar materials, and from an electrical perspective are difficult to integrate onto the same device (Table 2.1).

2.3.1 Problem 1: Band-Alignment

To obtain a high open-circuit voltage and short-circuit current, the band alignment at the silicon heterojunction should be precise.

As discussed before, in silicon heterojunction solar cells, one heterojunction blocks the majority carriers but lets the minority carriers through, and another blocks the minority carriers but lets the majority carriers through. For example, the heterojunction shown in Fig. 2.2(a), blocks electrons at the anode and holes at the cathode, to reduce dark current and enable high V_{OC} , but allows collection of holes and electrons at the anode and the cathode, respectively, so that photocurrent is high.

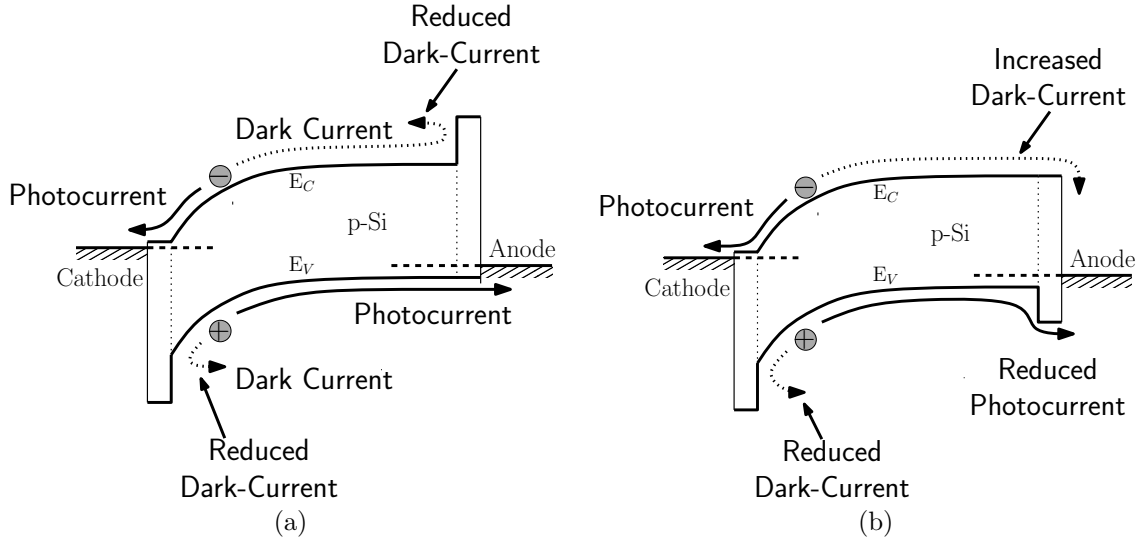


Figure 2.2: (a) Ideal wide-bandgap p-Si/organic heterojunction that blocks majority carriers (holes) at cathode and minority carriers (electrons) at anode. (b) A misaligned heterojunctions which blocks carriers at the wrong anode, leading to poor collection of photogenerated carriers.

If the strict alignment criteria is not obtained, device performance can suffer. For example, if holes are blocked at the anode (Fig. 2.2(b)), photogenerated holes are not efficiently collected and short-circuit current will be reduced. This is one of the issues in HIT cells [52]. Another issue could arise when a desirable barrier is not high enough, e.g in Fig. 2.2(b) the electron barrier at anode is not high enough to sufficiently reduce the dark-current, leading to a lower V_{OC} .

The good news is that unlike the aSi/cSi heterojunction, which can only use amorphous Si, silicon/organic heterojunctions have a virtually unlimited choice in organics. Leveraging the synthetic variety of organic semiconductors, band-alignment problems probably could be avoided. As we shall see in later chapters, in order to demonstrate efficient heterojunction cells, it is extremely important to identify and remedy band-alignment issues.

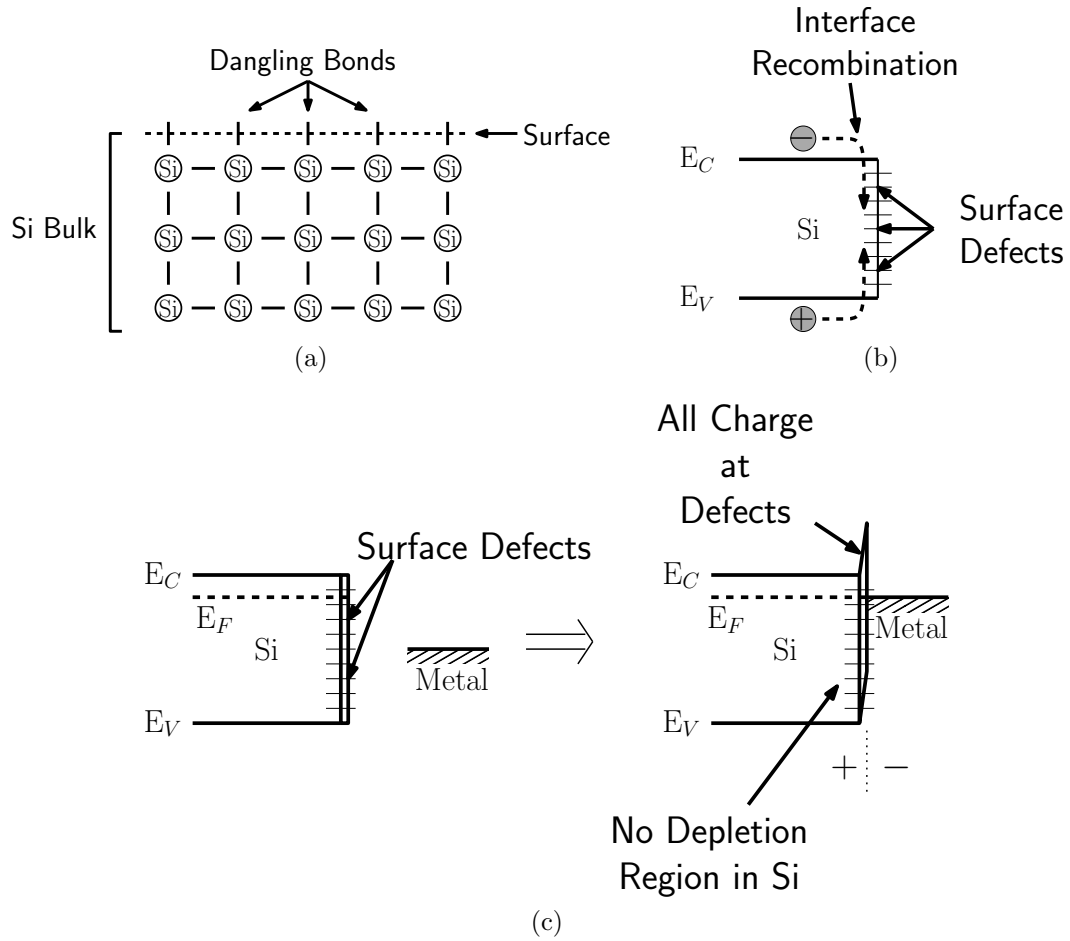


Figure 2.3: (a) Unsatisfied valencies, or “dangling bonds” at a un-passivated silicon surface. Surface defects cause (b) increased carrier recombination and (c) Fermi-level pinning, preventing modulation of surface energies.

2.3.2 Problem 2: Surface defects

One of the biggest problems at a silicon/organic interface is the presence of midgap defect states on the silicon surface.

At a pristine silicon surface, the symmetry of the silicon lattice is broken and some of the valencies of surfaces atoms are unsatisfied - called silicon “dangling” bonds (Fig. 2.3(a)). Typically the density of dangling bonds at pristine silicon surface is around 10^{14} cm^{-2} . Dangling-bonds may cause midgap defect-states at the silicon surface ($N_{\text{defect}} = 10^{11}\text{-}10^{13} \text{ cm}^{-2}$, depending on the surface passivation quality), which could degrade the device performance by increasing the carrier recombination [65]

(Fig. 2.3(b)). Furthermore, the large electric field at the Si/metal interface is required to separate the photogenerated carriers in SOH solar cells. The strength of the field, and hence the open-circuit voltage, might be affected if the Fermi-level is pinned near near midgap due to surface-defects (Fig. 2.3(c)).

When an organic is deposited on top of such an “unpassivated” Si surface, two problems can occur:

1. The organic molecule does not chemically interact with the Si dangling-bonds and some dangling-bonds remain on the Si/organic interface.
2. Organic molecules do chemically interact with the dangling-bonds, but the organic deposition is not epitaxial, i.e. organic molecules do not assemble in an ordered pattern over the underlying silicon lattice. This again leaves some unsatisfied dangling-bonds at the Si/organic interface.

These interface defects can render the heterojunction useless for photovoltaic applications. For example, consider a p-type-silicon/organic wide-bandgap heterojunction designed with a large offset at the conduction band to block electrons from recombining at the metal anode. If it has a large defect density at the interface that allows the carriers to recombine, any blocking effect of the heterojunction is nullified (Fig. 2.4a). Thus it is imperative that the silicon surface at the silicon/organic interface be well passivated.

One way to reduce the interface defect density is to passivate the silicon dangling bonds by an intermediate layer, deposited between silicon and organic. In this silicon/passivation/organic stack, the passivating layer is deposited first to consume the dangling bonds at the silicon surface, and then the organic layer is added on top of the passivating layer to engineer the desired electrical properties of the heterojunction (Fig. 2.4(b)).

Traditionally, layers of insulators like silicon dioxide or nitride are used to passivate

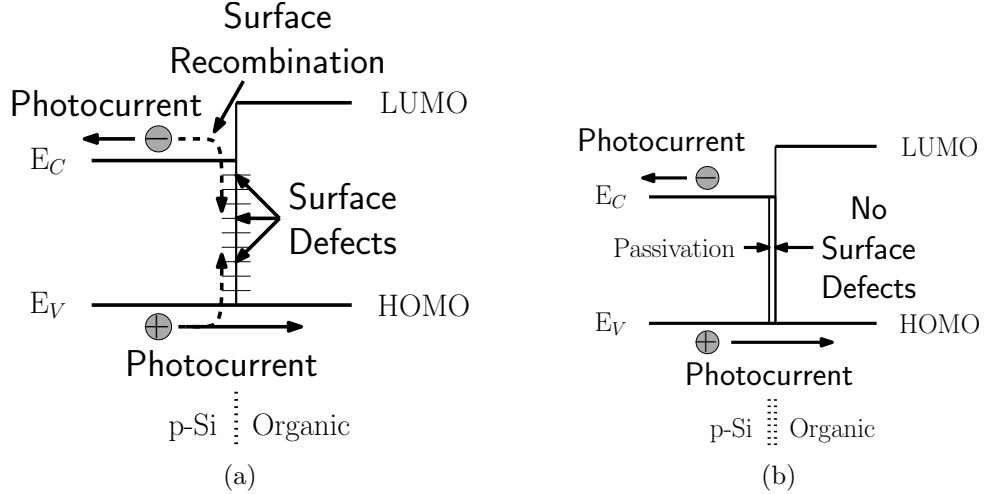


Figure 2.4: (a) Unsatisfied valencies, or “dangling bonds” at a unpassivated silicon surface cause recombination at Si/organic heterojunction. (b) A passivating layer reduces recombination, and organic layer sets the band-offsets.

silicon. While the performance of these passivating layers is very good ($<10^{11}$ cm $^{-2}$) [31], these layers are not useful for silicon/organic heterojunctions for two reasons. First, the deposition temperatures are too high (600 - 1000 °C) considering that the whole point is to reduce thermal budgets. Second, these insulating layers would not allow low-resistance current transport across the heterojunction [66, 67]. To enable high-quality silicon/organic heterojunctions, there is a need for a low-temperature deposited semiconducting passivation scheme.

There have been attempts to passivate the Si surface with more conducting materials, such as thin-film semiconductors. One of the successful examples is the amorphous-Si/crystalline-Si heterojunction used in the HIT cells (Section 1.6.2). Another way to passivate the silicon surface is through the use of chemicals, such as hydrofluoric acid (HF) for hydrogen-passivation [68] and I $_2$ /alcohol for iodine-passivation [69], Quinhydrone [70], etc. Using these treatments, very low surface recombination velocities of <100 cm/s (equivalent to surface defect density of only $\sim 10^{11}$ cm $^{-2}$) have been previously reported. However, these methods are not stable enough for use in practical devices.

Some groups have also attempted to passivate the silicon surface with organic materials, notably the Si(111) surface with alkyl chain derivatives [71, 72, 73, 74] but alkyl chains typically are insulating and would block the path of photocurrent. There are no reports of organic-passivated silicon solar cells.

There is a need for a low-temperature method to passivate the silicon/organic interface. In this thesis a novel organic-based passivation scheme was developed for precisely this purpose (Chapter 3).

2.4 Silicon/Organic Heterojunction to Block Minority Carriers at the Anode

An organic semiconductor that can reduce recombination of minority carriers at the p-silicon/metal contacts, like the one that blocks electrons at the anode (Fig. 2.5(c)), needs to satisfy two specific band-alignment criteria:

- (a) The LUMO of the organic should be much higher than conduction band edge of silicon, i.e. there should be a large conduction band offset, so that electrons are repelled away from the surface,
- (b) The HOMO of the organic and valence bands edge of silicon should be aligned, i.e. there should almost no valence band offset, so that photogenerated holes can be efficiently extracted at the anode.

As discussed in the previous section, the presence of defects states at the silicon/organic interface could reduce the efficacy of the blocking effect of the heterojunction. Thus it is imperative that the silicon surface at the silicon/organic interface be well passivated. Furthermore there should not be any “ E_V /HOMO” offset, otherwise the photocurrent will be reduced (Fig. 2.5(d)).

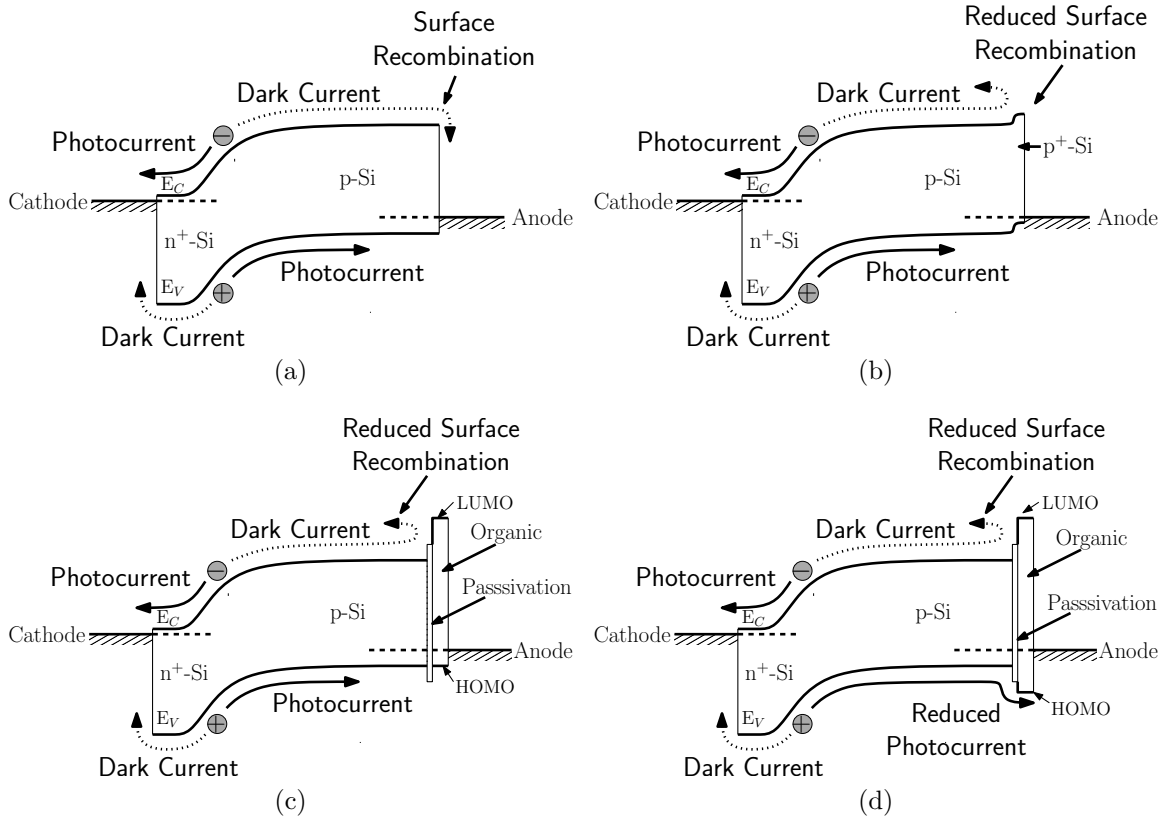


Figure 2.5: (a) Band Diagram of solar cell in which recombination at the metal contact dominates. The solid lines are desired direction of photogenerated carrier flow and the dashed line represents dark current, or equivalently the loss mechanism. (b) Solar cells with a p/p^+ back surface field to reduce electron recombination at the anode. (c) Solar cells with a silicon/organic heterojunction back surface field to reduce the electron recombination at the anode due to the offset in the conduction band. (d) A poorly designed heterojunction with a non-zero “ $E_V/HOMO$ ” offset, so that hole photocurrent is also blocked.

2.4.1 Closed-Form Expression of Minority Carrier Current in Heterojunction

To get a qualitative number of how high a surface recombination velocity can be tolerated, analytical closed-form expressions were used to estimate the effect of non-zero recombination velocity at the Si/organic interface.

The closed form expression for the electron current in the $n-p$ structure (Fig. 2.5(a))

in short-base condition is given by (Appendix A.3)

$$J_{e,n-p,SB} = -q \frac{n_i^2 D_{n,P}}{G_P} (e^{qV/kT} - 1) \quad (2.1)$$

where, G_P is the p-Si layer Gummel number, $D_{n,P}$ is the diffusion coefficient of electrons in p-Si layer, and V is the applied voltage. For Fig. 2.5(b), the expression for electron current changes to (Appendix A.4)

$$J_{e,n-p-p^+,SB} = -q \frac{n_i^2}{G_P/D_{n,P} + G_{P^+}/D_{n,P^+}} (e^{qV/kT} - 1) \quad (2.2)$$

where, G_{P^+} is the p^+ layer Gummel number, D_{n,P^+} is the diffusion coefficient of electrons in p^+ -Si layer. Due to the surface field of the p/p^+ junction the currents in the $n-p-p^+$ diode are lower than than the $n-p$ diode by a factor of

$$\frac{J_{e,n-p-p^+,SB}}{J_{e,n-p,SB}} = \frac{1}{1 + \frac{G_{P^+} D_{n,P}}{D_{n,P^+} G_P}} \quad (2.3)$$

The current reduction achieved with a 1- μm thick 10^{19}-cm^{-3} doped $p-p^+$ junction layer on 10^{16} cm^{-3} p-type substrate of 200 μm thick

$$\frac{J_{e,n-p-p^+,SB}}{J_{e,n-p,SB}} = \frac{1}{76}$$

For the device with an electron-blocking heterojunction as back-surface field (Fig. 2.5(c)), the analysis is more involved (Appendix A.5), but for a short-base diode with surface recombination velocity at the Si/organic interface ($S_{si,org}$) and a conduction band offset (ΔE_C), the expression for the electron current is given by (A.54)

$$J_{n,n-p-org} = -q \frac{n_i^2}{G_P} \left[\frac{1}{1 + \frac{L_{n,P}}{\beta W_P}} \right] (e^{qV/kT} - 1) \quad (2.4)$$

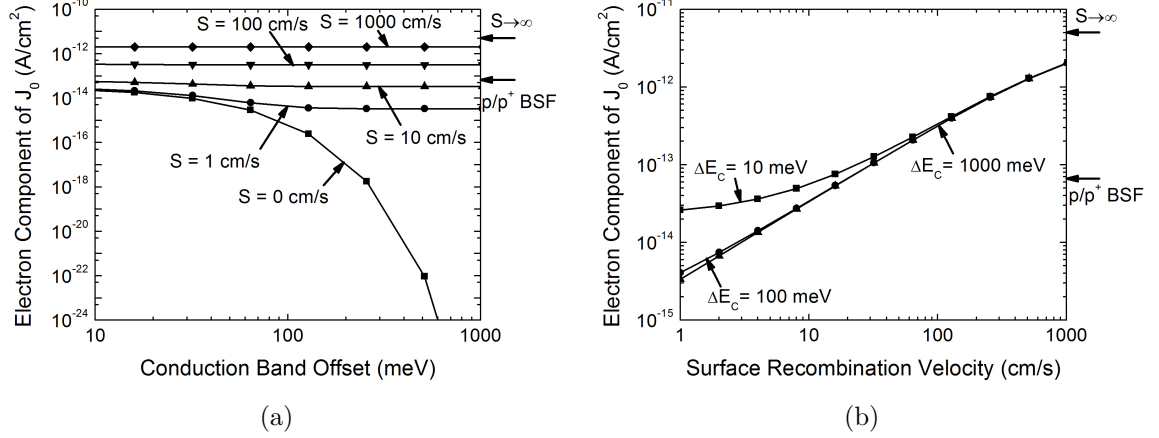


Figure 2.6: Electron component of J_0 of a n^+ - p Si diode with a Si/organic heterojunction BSF as a function of (a) conduction-band offset and (b) Si/organic interface recombination velocity. The substrate is 200 μm thick 10^{16} cm^{-3} doped p-type wafer. For reference the J_0 of a typical p-p⁺ back surface field (1 μm thick 10^{19} cm^{-3} doped) is also given. The heterojunction is very insensitive to barrier heights (for SRV > 1 cm/s) but very sensitive to surface recombination velocity.

where

$$\beta = \frac{\frac{D_{n,org}}{W_{org}} \frac{N_{C,org}}{N_{C,P}} \exp\left(-\frac{\Delta E_C}{kT}\right) + S_{Si,org}}{\frac{D_{n,P}}{L_{n,P}}} \quad (2.5)$$

$N_{C,P}$ and $N_{C,org}$ are the conduction band density of states for the silicon and organic layer, respectively. In all calculations it is assumed that $N_{C,P} = N_{C,org} = 10^{19} \text{ cm}^{-3}$.

Compared to a short-base diode without any back-surface field, the current reduction achieved by the heterojunction surface field is:

$$\frac{J_{n,n-p-org,SB}}{J_{n,n-p,SB}} = \frac{1}{1 + \frac{L_{n,P}}{\beta W_P}} \quad (2.6)$$

The plots of currents in a diode with heterojunction BSF as function of conduction band offset and surface recombination velocity, as predicted by (2.4), are given in Fig. 2.6. Due to negative exponential dependence of current on ΔE_C , the current

is very insensitive to changes in ΔE_C if $S_{si,org} > 1$. In terms of device design this indicates that to increase the performance of a heterojunction back-surface field, it is less important to increase the band-offsets and more important to achieve low surface recombination velocity at the Si/organic interface.

By comparing currents in a heterojunction back-surface field with currents in a typical homojunction back-surface field (1 μm thick 10^{19} , cm^{-3} p-type doped), it can be seen that the heterojunction surface field outperforms homojunction surface fields only when the surface recombination velocity at Si/organic interface is below 20 cm/s - a very low number (Fig. 2.6). This highlights both the importance of passivation and the technical challenge of fabricating a minority carrier-blocking Si/organic heterojunction.

2.5 Silicon/Organic Heterojunction to Block Majority Carriers at Anode

One of the simplest low-temperature replacements for p-n homojunction, for creating an electric field to separate electrons and holes, is the ‘‘Schottky’’ junction. For solar cells made on n-type silicon, the Schottky diode is fabricated by depositing a metal with high work-function (palladium, gold, platinum, etc) on silicon. The Schottky junction, too, has a built-in electric field which can separate electrons and holes, generating a high photocurrent (Fig. 2.7(b)). However, Schottky junctions are not used in solar cells because the silicon/metal barrier is not as effective, as a p-n junction, in blocking the majority carrier current. Consequently, the J_0 of a Schottky device is much higher ($>10^{-7}$ A/cm²) [32, 75] and the open-circuit voltage of a Schottky device is much lower (only ≈ 0.3 V) than a p-n junction [76].

The addition of an electron-blocking silicon/organic heterojunction can reduce the flow of electrons from silicon to anode, dramatically improving the photovoltaic

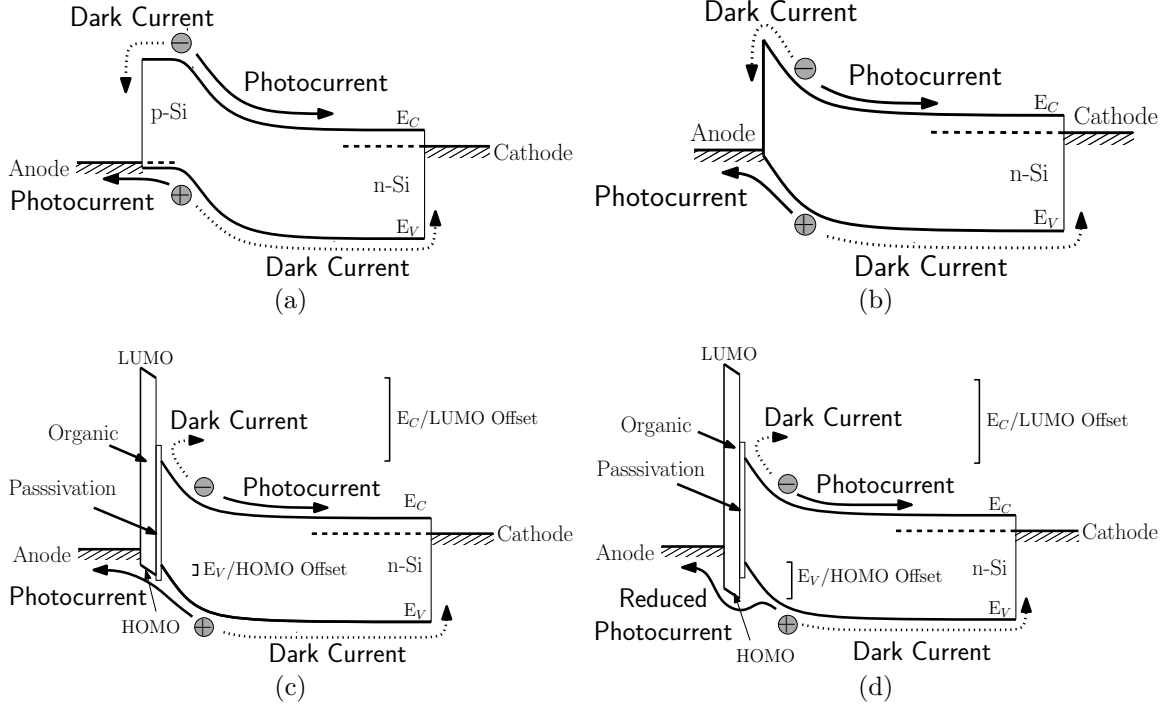


Figure 2.7: Band diagram of a (a) p-n junction and (b) Si/metal Schottky solar cell. The solid lines are desired direction of generated carrier flow and the dashed line represents dark current, or equivalently the loss mechanism. (c) An electron-blocking silicon/organic heterojunction with lower J_0 than Schottky junction. (d) A poorly designed heterojunction with a non-zero “ E_V /HOMO” offset, so that photocurrent is also blocked.

performance of the Schottky barrier device (Fig. 2.7(c)). Just as in Section 2.4, the organic semiconductor should have a wider energy-gap than silicon (1.1 eV) and the LUMO of the organic should be much above the conduction band minimum (E_C) of Si. This “ E_C vs. LUMO” offset reduces the flow of electrons from silicon to anode, leading to a lower J_0 and hence a larger V_{OC} . However, to maintain the short-circuit current, the organic layer must not block the photogenerated holes traveling from silicon to anode (Fig. 2.7(d), illustrates the counter example). So the hole barrier, given by the “ E_V vs. HOMO” offset, should be very small, i.e. the HOMO of the organic should also be very close to valence band maximum (E_V) of the silicon. Finally, to minimize resistive losses, the hole mobility of the organic layer should also be reasonably high.

Due to the lower density of states, large band tails and wide energy-gap, the concept of Fermi-level in an undoped organic is ill-defined []. To a first order, the strength of the built-in field in silicon is decided by the difference in work-functions of silicon and top-metal. One way to think about the role of organic is as an undoped thin-layer of semiconductor sandwiched between two doped materials, metal on one side and silicon on the other. In such a scenario, the selection of metal is very important, e.g. to set a built-in field in a heterojunction on n-type silicon the anode work function needs to be high (metals such as Pd, Au, Pt, etc).

2.5.1 Closed-Form Expression of Majority Carrier Current in Heterojunction

Quantitatively, how much more effective is the electron barrier at the Si/organic heterojunction in blocking electrons in silicon from reaching the metal anode in forward-bias (as in Fig. 2.7(c))? The answer is, a lot. As the closed form expressions derived in the next subsection will show, compared to the p-n junction and Schottky diode devices (Fig. (a)-(b)), electron currents are lower in the heterojunction diode (Fig. 2.7(c)) by several orders of magnitude.

For a p⁺-n junction (Fig. 2.7(a)), the electron current going from n-Si to anode in Forward-bias is given as

$$J_{n,p-n} = q \frac{n_i^2 D_{n,P^+}}{G_{P^+}} (e^{qV/kT} - 1) \quad (2.7)$$

where, D_{n,P^+} is the electron diffusion coefficient in p⁺-Si layer, and G_{P^+} is the Gummel number of the p⁺-Si layer.

An analytically-derived expressions for electron current in Schottky-barriers is

given in Appendix A.6. For a general Schottky junction diode (Fig. 2.7(b))

$$J_{n,si-metal} = \frac{qN_{C,si}s_{metal}}{1 + \frac{s_{metal}}{s_{depSi}}} \left[\exp\left(-\frac{q\phi_{bn}}{kT}\right) \right] (e^{qV/kT} - 1) \quad (2.8)$$

where $N_{C,si}$ is the conduction band density of states in silicon, T is the temperature, k is the Boltzmann constant, V is the applied voltage, ϕ_{bn} is the metal-silicon barrier height. s_{metal} and s_{depSi} are the effective surface recombination velocities associated with the Si/metal interface and the transport of electrons from the edge of depletion region in silicon to the Si/organic interface, respectively.

$$s_{metal} = \frac{A^*T^2}{qN_C} \quad (2.9)$$

$$s_{depSi} = \frac{qD_{n,si}}{kT} \mathcal{E} \quad (2.10)$$

where \mathcal{E} is electric field in Si at the interface. At 300°K, $s_{metal} \sim 9 \times 10^6$ cm/s. For a Schottky diode fabricated on 10^{16} doped wafer with $\phi_{bn} = 0.9$ eV, $s_{depSi} \sim 3 \times 10^7$ cm/s at a 0.5 V forward bias. Since $s_{depSi} > s_{metal}$, the current equation reduces to

$$J_{n,si-metal} \approx qN_{C,si}s_{metal} \left[\exp\left(-\frac{q\phi_{bn}}{kT}\right) \right] (e^{qV/kT} - 1) \quad (2.11)$$

Comparing the current from the Schottky junction diode with electron current of the p⁺-n junction diodes,

$$\frac{J_{n,si-metal}}{J_{n,p-n}} = \frac{N_{C,si}s_{metal}G_{P^+}}{D_{n,P^+}n_{i,si}^2} \left[\exp\left(-\frac{q\phi_{bn}}{kT}\right) \right] \quad (2.12)$$

$$> 10000 \quad (2.13)$$

the currents in Schottky diodes are higher by a factor of more than 10000, even with a relatively large Si/metal barrier of 0.9 eV. The calculation assumes $G_{P^+} = 10^{15}$ cm⁻² and $D_{n,p^+} = 2$ cm²/s (1 μm thick 10^{19} cm⁻³ doped p⁺ layer), which are usual values in

practical solar cells. Therefore, the Si/metal device is never used in solar cell.

For the Si/organic/metal device (Fig. 2.7(c)) the expression for current in the Schottky diode (A.64) can be generalized to

$$J_{n,si-organic-metal} = \frac{qN_{C,org}s_{siorg}}{1 + \frac{s_{siorg}}{s_{depOrg}}} \left[\exp \left(-\frac{q\phi_{bnerg}}{kT} \right) \right] (e^{qV/kT} - 1) \quad (2.14)$$

where $N_{C,org}$ is the conduction band density of states in organic, ϕ_{bnerg} is the metal-organic barrier height. s_{siorg} and s_{depSi} are the effective surface recombination velocities associated with the Si/organic interface and the transport of electrons from the edge of depletion region in silicon to the Si/metal interface, respectively.

Assume that the electric field induced in silicon is simply a function of the metal work function, so that the values of \mathcal{E} and s_{depSi} remain the same ($\sim 10^6$ cm/s) for the Si/metal and the Si/organic/metal devices. This is reasonable assumption for very thin organic layers. On the other hand, $s_{siorg} < s_{metal}$, because no matter how unpassivated the Si/organic interface is, it can't be worse than Si/metal interface. Usually s_{siorg} is less than 10^4 cm/s. So

$$s_{siorg} \ll s_{depSi} \quad (2.15)$$

and the expression for current reduced to

$$J_{n,si-organic-metal} = qN_{C,org}s_{siorg} \left[\exp \left(-\frac{q\phi_{bnerg}}{kT} \right) \right] (e^{qV/kT} - 1) \quad (2.16)$$

Compared to the p⁺-n junction (assuming $G_{P^+}=10^{15}$ cm⁻² and $D_{n,p^+}=2$ cm²/s), the electron current reduction achieved by the heterojunction with a barrier (ϕ_{bnerg})

of 2 eV, s_{siorg} of 1000 cm/s and $N_{C,org}$ of 10^{19} cm⁻³ is

$$\frac{J_{n,si-organic-metal}}{J_{n,p-n}} = \frac{N_{C,org} s_{siorg} G_{P^+}}{D_{n,P^+} n_{i,si}^2} \left[\exp \left(-\frac{q\phi_{b,org}}{kT} \right) \right] \quad (2.17)$$

$$< 10^{-17} \quad (2.18)$$

This is a very low number for electron current that probably will never be measured in practice. However, the basic point stands - the barrier height at the Si/organic heterojunction is so large (~ 2 eV) that reductions achieved in the majority carrier current in Si/organic heterojunctions are much larger than current reductions achieved with either Schottky or p-n junction diodes. One assumption implicit in this analysis, is that there exists a large depletion region in silicon. If the Fermi level in silicon is pinned at a lower level than what is implied by the barrier height, due to the Si/organic surface defects, the reduction in the electron current will be lower.

Finally, a crucial difference between the heterojunction presented here and the one presented in the last section (Section 2.4) needs to be clarified. While both block electrons, there are subtle differences. First, the minority-carrier blocker improves the performance of solar cells, but on its own cannot generate photocurrent. The majority carrier blocker of this section, however, can form a complete solar cell on its own. Second, the minority-carrier blocking heterojunction of previous section is more susceptible to surface recombination at the Si/organic interface, and hence is a tougher problem to solve (See Fig. 2.6b). This was hinted by the closed form expressions in the two cases, where it was noted that while the minority-carrier current through the minority-carrier blocker is strongly affected by the surface recombination velocity ($S_{si,org}$) but is mostly independent of band-offsets at the Si/organic interface, the majority-carrier current through the majority-carrier blocker is overwhelmingly decided by the barrier height ($\phi_{b,org}$) and only weakly dependent on the surface

recombination velocity of the Si/organic interface.

2.6 Conclusion

In the absence of a crystalline wide-bandgap heterojunction for silicon, silicon/organic heterojunctions are useful for a range of applications: from sensors to solar cells. Such hybrid devices are expected to have both performance and cost advantages over homojunction devices, but some critical challenges need to be identified and solved first. In this chapter we identified two of the critical issues and presented designs of two heterojunctions that are useful for Si/organic hybrid solar cells.

The first critical issue is designing the band-offsets at the Si/organic interface. Poorly designed band-offsets at the silicon/organic interface can reduce the photocurrent, negating any advantage of lower recombination. A second, and potentially bigger issue, in integrating the amorphous organic layers on crystalline silicon, are interface defects due to silicon dangling bonds. The surface defects increase recombination and pin the Fermi-level, both of which degrade device performance. The established methods/layers to passivate the surface defects are not useful for heterojunctions, either due to their high resistance or lack of long-term stability. There is a need for a new passivation scheme for crystalline silicon where the passivating layer can be deposited at low-temperatures and is not insulating.

Two heterojunction designs have been presented that can be used to fabricate low-cost and efficient hybrid solar cells. The first heterojunction blocks the minority carriers from recombining at the Si/anode contact and the second blocks majority carriers from reaching the Si/anode contact under forward-bias. Analytical expressions derived from first principles prove that heterojunctions can be used to improve the performance of conventional homojunction solar cells. It is envisioned that these two heterojunctions can be integrated on the opposite sides of a single device to make

efficient room-temperature processed silicon solar cells.

Chapter 3

Silicon Surface Passivation by 9,10-Phenanthrenequinone

3.1 Introduction

One of the critical challenges of silicon/organic interfaces is the presence of midgap defects due to silicon dangling-bonds. In this chapter, a novel organic-based passivation scheme for the silicon (100) surface is presented. The passivation precursor is a cheap and easily available organic small molecule, 9,10-phenanthrenequinone (PQ) (Fig. 3.4) [77, 13, 12, 14]. Passivation is achieved by thermally evaporating a thin layer of PQ on to silicon. During deposition, the silicon is maintained at room-temperature. Once passivated by PQ, further organic layers can be deposited on top of silicon to form a silicon/organic heterojunction.

Minority carrier lifetime measurements show surface defect densities of only $\sim 10^{11}$ cm^{-2} at the PQ-silicon interface, rivaling the electronic quality of silicon-dioxide passivated Si surfaces. X-ray Photoelectron Spectroscopy (XPS) measurements show that PQ passivates the surface by reacting with the surface silicon atoms by a cycloaddition “redox” process. The measured band-bending at both n and p-type PQ-passivated

silicon surfaces is lower than band-bending at hydrogen passivated silicon surface, presumably because PQ consumes the silicon dangling bonds which are responsible for surface defects. Ultra-violet and inverse photoelectron spectroscopy (UPS, IPES) are used to investigate band alignment at the PQ-silicon interface for both p- and n-type silicon, which is important to understand charge transport properties of the interface. Further, measurements of metal-insulator-PQ-silicon devices prove that the Fermi-level at the PQ-passivated silicon surface is not “pinned” and can be modulated over a wide energy range. Overall we infer that the silicon/PQ interface is remarkably “ideal” - free from electrically active interface defects and Fermi-level pinning - and can be used in hybrid devices as a passivating intermediate layer between silicon and organic semiconductors.

The surface science measurements in this chapter (XPS, UPS, and IPES) were made in collaboration with Dr. Yabing Qi of Prof. Kahn’s research lab.

3.2 Comparison with Other Passivation Schemes

Other groups have attempted to passivate the silicon surface with organic materials, notably with alkyl chains derivatives[71, 72]. The work here differs in several critical aspects. First, a very high degree of electronic perfection (defect density of only $\sim 10^{11}$ cm⁻²) has been achieved on the silicon surface with an organic molecule, permitting Fermi-level modulation. Second, alkyl chains are inherently insulating, while PQ maintains aromaticity after bonding to the silicon surface. This should enable efficient charge transport across the organic-silicon interface, which is important for devices such solar cells and bipolar transistors. Third, while most of the previous work has focused on the Si (111) surface, we demonstrate excellent passivation of the silicon (100) surface, which is more commonly used in conventional silicon technology.

Ultra-thin oxides, that allow carriers to tunnel through, can also be used to obtain

a passivated and conducting Si surface. However, the resistive losses in these devices are known to be high [67].

Another way to passivate the silicon surface is through use of chemicals, such as hydrofluoric acid (HF) [68] and I₂/alcohol [69], quinhydrone [70], etc, which passivate the silicon surface by forming Si-H, Si-I, bond, etc. Using these treatments, very low surface recombination velocities of <100 cm/s (equivalent to surface defect density of only 10¹¹ cm⁻²) have been previously reported. In this project experiments were conducted to passivate silicon using these schemes but the results were not encouraging due to poor stability of the passivation (for both H- and I₂-passivation) and concerns about compatibility of organic and passivating layer (in the case of I₂-passivation).

3.3 Materials and Equipment

PQ and iodine were purchased from Sigma Aldrich at the highest available purity (typically >99%) and used as is. CMOS grade chemicals from JT Baker were used for wafer cleaning.

Prior to passivation, the silicon (100) wafers were first cleaned by rinsing with acetone, methanol and 2-propanol in an ultrasonic bath for 10 minutes each. Next, trace organic contaminants were removed by the SC-1 step of the standard RCA clean : ammonium hydroxide + hydrogen peroxide + DI water (1:1:5) at 80 °C for 15 minutes then rinse [78]. This was followed by 1:100 hydrofluoric acid for 1 min to remove the native-oxide. Finally trace metal contaminants were removed with the SC-2 step of the RCA clean: hydrogen chloride + hydrogen peroxide + DI water (1:1:5) at 80 °C for 15 minutes then rinse [78]. Instead of the two-step RCA clean, sometimes a single step Piranha clean was used: Sulfuric Acid + hydrogen peroxide (1:4) at 80 °C for 15 minutes then rinse [78]. Lastly, the wafers were dipped in a 1:100 aqueous hydrofluoric acid solution for 1 min to strip the native oxide layer. The

resulting hydrogen-passivated Si wafers were then passivated by one of the methods mentioned in later sections. No specific measures were undertaken to de-oxygenate the cleaning solutions.

Minority carrier recombination lifetimes were measured by the quasi-steady-state photoconductance (QSSPC) method using a commercial instrument (WCT-120) manufactured by Sinton Consulting, Boulder, CO [79]. All the spectroscopic analyses was done in Prof. Kahn's lab in a separate ultra-high vacuum (UHV) chamber (base pressure $<2 \times 10^{-10}$ Torr). During transport to the UHV chamber, test samples were exposed to air for no more than 5 minutes. Electrical measurements of devices were done using the 4155B semiconductor parameter analyzer and HP 4175 LCR meter.

3.4 Minority Carrier Lifetime Measurement

The rate at which minority-carriers recombine is an excellent measure of the electrical quality of a semiconductor surface. As mentioned before, midgap defects due to the dangling bonds at a semiconductor surface act as minority-carrier recombination centers. Moreover these defects may carry charge, causing the bands near the surface to bend towards the mid-gap. The resulting electric field at the surface attracts even more minority-carriers, exponentially increasing the rate of carrier recombination [80].

The minority carrier recombination rate is characterized by a recombination lifetime (τ_r) which, in low-level injection, depends on the recombination rate (U) and excess minority-carrier density (n'_{min}) as

$$U = \frac{n'_{min}}{\tau_r} \tag{3.1}$$

3.4.1 Effect of Surface Recombination

In a semiconductor with no surface defects, recombination only proceeds via the bulk defects. The measured (or *effective*) recombination lifetime (τ_{eff}) is simply the bulk recombination lifetime (τ_{bulk}).

$$\frac{1}{\tau_{eff}} = \frac{1}{\tau_{bulk}} \quad (3.2)$$

As the density of electrically-active defects at the surface increases, additional minority-carriers are lost to surface recombination. This increase in carrier recombination rate is observed as a decrease in the effective minority-carrier lifetime [81].

$$\frac{1}{\tau_{eff}} = \frac{1}{\tau_{bulk}} + \frac{1}{\tau_{surface}} \quad (3.3)$$

where $\tau_{surface}$ is the lifetime associated with surface recombination. How much the effective lifetime (τ_{eff}) differs from the bulk value (τ_{bulk}), gives a qualitative estimate of the surface quality.

3.4.2 Quasi Steady-State Photoconductance Decay

Photoconductance decay (PCD) is a class of methods that measure minority-carrier recombination which can be made without making electrical contact to a semiconductor. This allows characterization of recombination properties in a system without the need to fabricate full devices with metal contacts. In this project, minority-carrier recombination lifetimes were measured using the WCT-120 system from Sinton Consulting, an instrument based on the Quasi-steady-state photoconductance decay (QSSPCD) method [79].

The quasi-steady-state PCD is a specific type of PCD experiment, in which the light source used has a slow decay rate (5-10 ms). If the lifetime of the samples being measured is smaller than the decay rate of the light source, which is usually

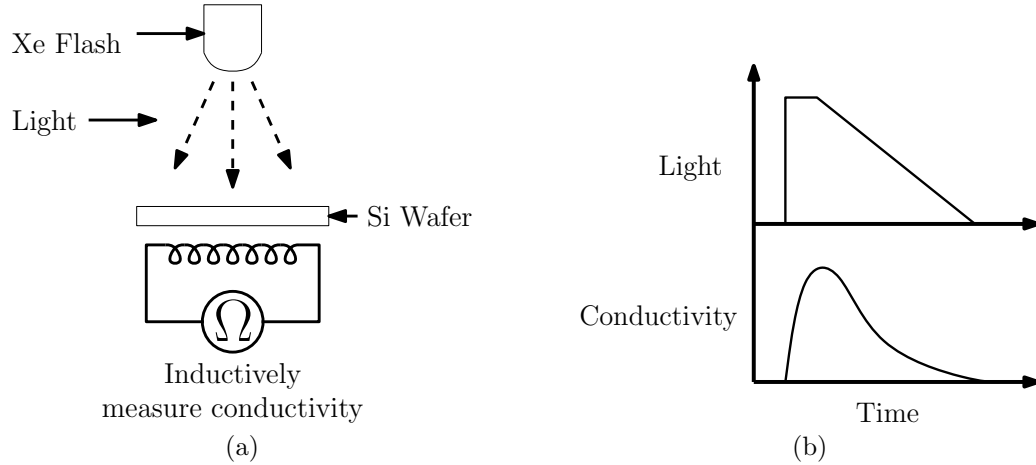


Figure 3.1: (a) The instrument schematic showing the main components, the light source, inductively coupled conductivity meter, and the silicon wafer to be tested. (b) Typical input and output waveforms in WCT120. The flash generated a slowly (5-10 ms) decaying light pulse. In response carriers are generated in silicon and the measured conductivity goes up. The rate of decay given the measure of recombination lifetime.

the case for wafers with recombination lifetime of less 1 μs , then at every point of the experiment the system can be assumed to be in quasi-equilibrium (hence the quasi steady state) [79].

The WCT-120 consists of a camera flash with a Xe bulb suspended over a sensor that is tuned to inductively measure the conductivity of a silicon wafer kept (Fig. 3.1(a)). The sensor is approximately an inch in diameter, so area-averaged value of lifetime is measured. To make a measurement, the silicon wafer is first placed over the sensor. The computer-controlled flash is then triggered. A calibrated diode measures the intensity of the light from the flash as a function of time, from which a photogeneration rate in silicon is calculated (G_{av} in cm^{-3}). The intense light from the Xe-flash (30-50 Suns) creates excess carriers in the silicon. These excess carriers cause a transient increase in the conductivity of the silicon (Fig. (b)). The measurement system records the change in the conductivity using an inductor placed below the sample, which is converted into a time dependent average excess minority-carrier density (Δn_{av} in cm^{-3}). As the generated carriers recombine, the excess carrier den-

sity falls back to its equilibrium value. Lifetime is extracted from the rate of change of the minority-carrier density and the photogeneration rate, using the generalized steady-state analysis [82]

$$\begin{aligned}\frac{d\Delta n_{av}(t)}{dt} &= G_{av}(t) - \frac{\Delta n_{av}(t)}{\tau_{eff}(\Delta n_{av})} \\ \Rightarrow \tau_{eff} &= \frac{\Delta n_{av}(t)}{G_{av}(t) - \frac{dn_{av}(t)}{dt}}\end{aligned}\quad (3.4)$$

Detailed derivation is discussed in Appendix B.

3.4.3 Relation Between s and $\tau_{surface}$

Surface recombination is more usefully described in terms of the surface recombination velocity (SRV, s in cm/s) because it has direct relation with the surface defect density. For a neutral surface, i.e. in absence of band-bending, SRV relates to the surface defects density (N_t) as

$$s = v_{th}\sigma N_t \quad (3.5)$$

where v_{th} is the carrier thermal velocity and σ is the defect capture cross-section [81, 80]. Surface defects can act as minority-carrier recombination centers with recombination rate U (in $\text{cm}^{-2}\text{s}^{-1}$) and for p-type substrates

$$U = sn'_{min,s} \quad (3.6)$$

where $n'_{min,s}$ is the excess minority-carrier density at the surface.

Without any illumination (no photogeneration, $G = 0$), a silicon wafer with thickness t and surface recombination only at top surface (SRV s at top and zero at the bottom surface), as shown in Fig. 3.2, has a $\tau_{surface}$ that satisfies

$$\tau_{surface} = \frac{1}{\beta^2 D_n} \quad (3.7)$$

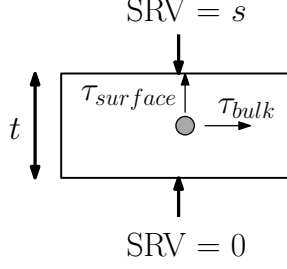


Figure 3.2: The effect of surface recombination on the measured *effective* minority-carrier recombination. Surface recombination is assumed on only one side of the wafer.

where D_n is the minority-carrier diffusion coefficient and β satisfies the transcendental equation

$$\tan(\beta t) = \frac{s}{\beta D_n} \quad (3.8)$$

In the limit of high and low surface recombination

$$\tau_{surface}(s \rightarrow \infty) = \frac{4t^2}{\pi^2 D_n} \quad \& \quad \tau_{surface}(s \rightarrow 0) = \frac{t}{s} \quad (3.9)$$

The derivation for these equations and others common cases are discussed in detail in Appendix B.

When there is photogeneration ($G \neq 0$), the equations get more complicated. In the general case, the lifetime and SRV can be calculated from the excess minority carrier density ($\Delta n(x, t)$), using [82]

$$\frac{\Delta n_{av}(t)}{\tau_s(\Delta n_{av})} = \frac{1}{W} s_{front} \Delta n(0, t) + \frac{1}{W} s_{back} \Delta n(W, t) \quad (3.10)$$

where,

$$\Delta n_{av}(t) = \frac{1}{W} \int_0^W \Delta n(x, t) dx \quad (3.11)$$

$$G_{av}(t) = \frac{1}{W} \int_0^W G(x, t) dx \quad (3.12)$$

$$(3.13)$$

s_{front} and s_{back} are recombination velocities at front and back surfaces, respectively. W is the wafer thickness. To rigorously extract the recombination velocities s_{front} and s_{back} from the τ_{eff} , the exact values of excess minority-carriers at the boundaries are needed, something that cannot be extracted from the data analytically. A method to numerically solve these equations given a light spectrum is discussed in Appendix B.

3.5 Silicon Surface Passivation by Wet Chemicals

Two wet chemical passivation methodologies were tested: hydrogen passivation [68] and iodine/methanol passivation [69]. The last step of the cleaning procedure, described in Section 3.3, already yields a hydrogen-passivated silicon surface. For I₂-passivation, the hydrogen-passivated samples were dipped in a 0.0005 M solution of I₂ in methanol for 1 minute, followed by a propanol-2 rinse.

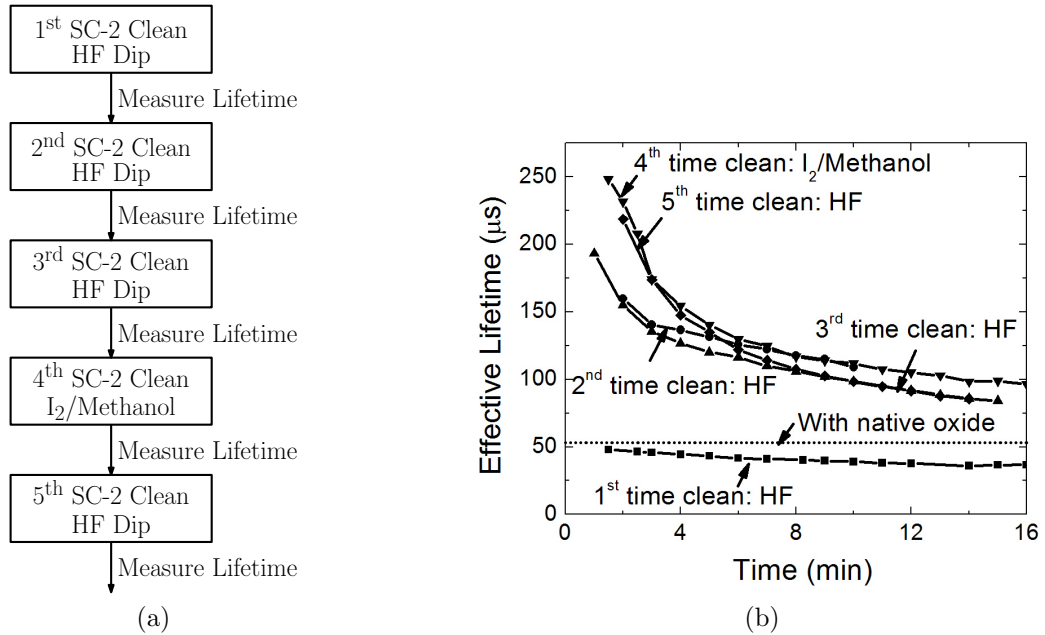


Figure 3.3: (a) The process flow of the experiment to characterize the H- and I₂-passivation schemes. (b) The evolution of carrier lifetime with time for different process steps.

To test the passivation quality, stability and repeatability of the H- and I₂-

passivation schemes, a high-lifetime unintentionally-doped p-type FZ Si (100) wafer (resistivity $>10 \text{ k}\Omega\text{cm}$) was repeatedly cleaned using the SC-2 step of the RCA procedure and passivated using either hydrogen or I_2 (Fig. 3.3(a)). The carrier lifetime of the passivated wafer was measured in air multiple times after each cleaning steps so as to chart the evolution of passivation quality over time (Fig. 3.3(b)). From the data we can draw the following conclusions:

1. Both passivation schemes passivate the silicon (100) surface.
2. However, neither of the passivation schemes is stable in air for more than 10-20 minutes. Over time the lifetime starts reverting back towards the baseline value of $53 \mu\text{s}$ - the lifetime measured for unpassivated wafers with native oxide. Since this is too short a time for photovoltaic operation, alternative passivation schemes will be required for silicon/organic heterojunction solar cells.
3. The rate of degradation is the almost same in both schemes, but at least in this run I_2 -passivation gave higher lifetimes, i.e. I_2 passivates silicon better than hydrogen.
4. The lifetime of a new wafer taken right out of the box is substantially lower than the what is measured from the second clean onwards, e.g. The lifetime after 1st cleaning was only $50 \mu\text{s}$, but after 5th cleaning step it was $250 \mu\text{s}$. Arguably this is due to sawing and polishing damage that is always present on polished wafers. Once the top few nm of the silicon are consumed, due to successive oxidation and etching steps of the RCA clean, the surface damage is removed and higher lifetimes are achieved.

3.6 Silicon Surface Passivation by 9-10 Phenanthrenequinone

9-10-Phenanthrenequinone (PQ) is a cheap and readily available organic small molecule that can be deposited on silicon by thermal evaporation. We investigated PQ on the suggestion of Prof. Jeff Schwartz of the Department of Chemistry. The interaction between PQ (Fig. 3.4) and a $[2\times 1]$ reconstructed silicon (100) surface (with silicon dimers) has been previously studied using spectroscopy and scanning tunneling microscopy [77]. In the study, the authors concluded that a) PQ reacts with the silicon (100) surface and b) the packing density of PQ on the silicon surface is high c) the reaction between PQ and Si maintains the π -conjugation, and hence the semiconducting property, of the PQ molecule - desirable properties for a passivating layer. No macro-scale lifetime or devices were tested which show electrical passivation but the study is interesting and inspired this work.

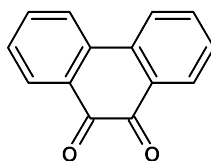


Figure 3.4: 9,10-phenanthrenequinone (PQ), the surface passivation precursor.

3.6.1 Method

The cleaned hydrogen-passivated samples were loaded into the vacuum chamber in room C405A (Angstrom Evaporator) and the chamber was pumped to the base pressure of 5×10^{-7} Torr. Pumping times were typically 1.5 to 2 hrs. Inside the chamber, the silicon surface was exposed to ~ 30 Langmuirs (1 Langmuir= 10^{-6} Torr·s) of thermally evaporated PQ vapor (vapor pressure $\sim 5\times 10^{-8}$ Torr), to give an estimated thickness of 10 nm. The dosage was calculated by multiplying the excess pressure

(evaporation pressure - base pressure) by the time of deposition. The thickness was estimated using a quartz crystal microbalance which was pre-calibrated by measuring a thicker 50-nm PQ film with a surface profilometer. However, even at room temperature PQ seems to evaporate off the silicon surface -the thickness of a PQ film stored in the evaporation chamber starts reducing - so the calibration is not expected to be exact. Tantalum boats were used to deposit PQ. The reaction between Si and PQ does not seem instantaneous (detailed discussion in Chapter 6), requiring hours to reach completion. Therefore after PQ deposition, samples were typically left in the chamber (under vacuum) for several hours before unloading.

3.6.2 Surface Recombination at the Si/PQ Surface

To test if PQ indeed passivates the silicon surface, the recombination lifetimes of p- and n-type PQ-coated Si wafers were measured by QSSPCD.

Measurements were taken on a 15 Ω -cm p-type boron-doped silicon (100) wafer with three different surface treatments; oxide, native-oxide, and PQ-passivated (Fig. 3.5(a)). With a coating of high-quality thermal oxide, grown at 1050 $^{\circ}\text{C}$, a lifetime of 107 μs ('oxide') was measured at a minority-carrier density of 10^{14} cm^{-3} (Table 3.1). Next, the oxide at the top surface was etched away and a native-oxide was allowed to form on the exposed silicon surface. The native-oxide/silicon interface is known to have a very high defect density, and hence the lifetime dropped to 12 μs ('native-oxide'). Finally, after etching away the native oxide, PQ was deposited on the bare silicon surface and the measured lifetime recovered to 78 μs ('PQ-passivated'). Similar results were also obtained for 3 Ω -cm phosphorus-doped silicon wafer at a minority-carrier density of 10^{15} cm^{-3} (Fig. 3.5(e)). The lifetimes measured for thermal-oxide, native-oxide and PQ-passivated n-Si surfaces were 192, 26 and 122 μs , respectively. In both cases, the lifetimes of PQ-passivated and thermal oxide coated wafers are comparable, demonstrating the passivation quality of PQ (Table 3.1).

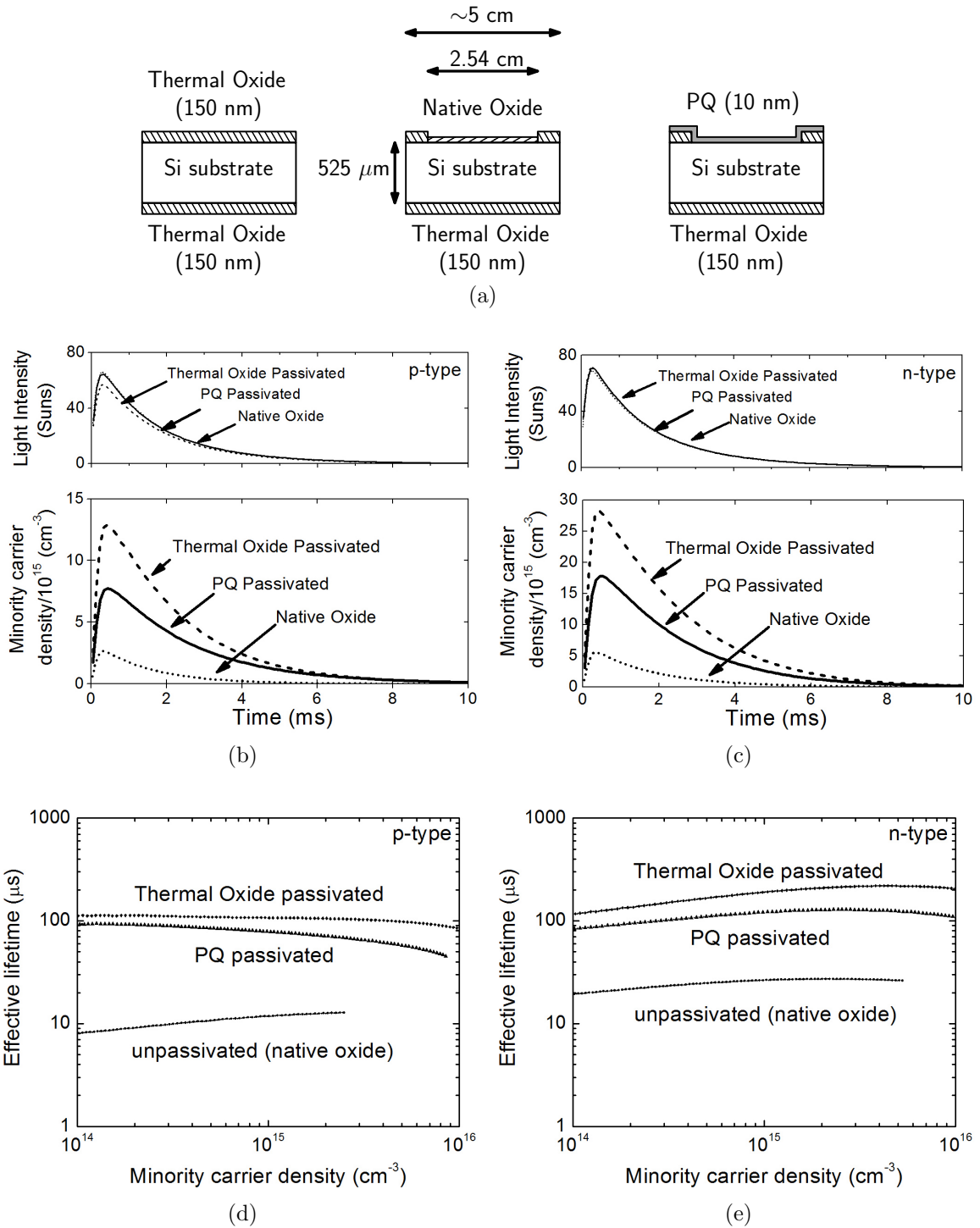


Figure 3.5: (a) The same test structure measured with three different surface treatments; thermal-oxide passivated, PQ-passivated, and unpassivated. Data output of the QSSPCD experiment for (b) p-Si and (c) n-Si samples. Effective Lifetime vs. minority-carrier density for (d) p-type and (e) n-type CZ silicon (100) wafer.

For a quantitative estimation of the surface defect density, the lifetime data was further analyzed in terms of surface recombination velocity. Hidden in the lifetime numbers are five unknown parameters: the bulk lifetime (τ_{bulk}), the thermal-oxide SRV at top (polished) surface ($s_{ox,front}$), the thermal-oxide SRV at back (rough) surface ($s_{ox,back}$), the PQ SRV at top surface (s_{PQ}), and the native-oxide at top surface ($s_{no,front}$). Assuming negligible band-bending, these five parameters can be calculated from τ_{eff} using the generalized QSSPCD analysis (Eq. (3.10)). Details about the calculations are explained in Appendix B.

The calculated values of bulk lifetime for p and n-type silicon substrates were 122 and 252 μ s, respectively. It is well-known that high-quality thermal-oxide/silicon interfaces are almost defect-free and hence very low SRV, less than 30 cm/s, were extracted for both type of substrates (Table 3.1). For the PQ-passivated p-type and n-type wafers recombination velocities of 145 and 133 cm/s, respectively, were calculated. In contrast, at the ‘native’ silicon surfaces, SRV of 4804 cm/s and 2014 cm/s are calculated for p and n-type substrates, respectively. Since PQ is deposited at low temperatures (< 100 °C), we can assume that τ_{bulk} remains unchanged for all the three surface treatments. Hence, any change in τ_{eff} is exclusively due to differences in τ_{surf} , which is directly affected by the surface defect density.

Assuming a thermal velocity of 10^7 cm/s and a capture cross-section of $\sim 10^{-16}$ cm², we estimate the defect density to be $\sim 10^{11}$ cm² for PQ-passivated surfaces; i.e., only 1 in 10,000 silicon atoms is unpassivated.

Finally, a note on stability and passivation procedure. It was observed that the quality of passivation varied from sample to sample. Preliminary studies were done to identify the factors that affect the quality and stability of PQ-passivated surfaces, some of which have been detailed in Chapter 6. However, the reasons for the observed variations are still unknown.

Table 3.1: The measured minority-carrier recombination lifetimes in silicon at a minority-carrier density of 10^{15} cm^{-3} and extracted surface recombination velocity (SRV) [82] in p and n-type substrates. The three conditions represent different surface treatments; passivated with a high-quality thermal oxide, unpassivated (native oxide), and PQ-passivated.

	τ_{eff} at carrier density of 10^{15} cm^{-3} (μs)			SRV (cm/s)		
	Oxide	Native Oxide	PQ-passivated	Oxide	Native Oxide	PQ-passivated
p-type	107	12	78	9	4804	145
n-type	192	26	122	26	2014	133

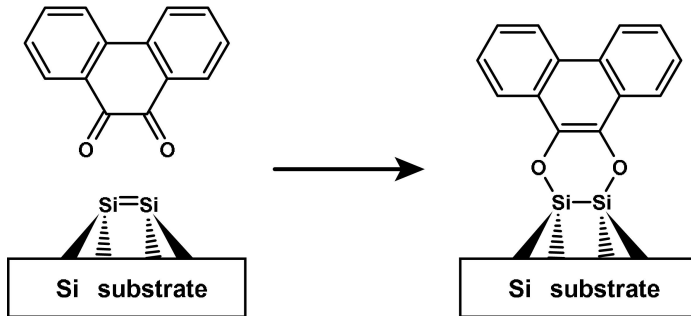


Figure 3.6: The proposed reaction between PQ and reconstructed silicon (100) surface with silicon dimers [77]. The reaction consumes the dimer while preserving the aromatic π -conjugation of PQ.

3.6.3 Spectroscopic Analysis of the Si/PQ Interface

Previous Study of Silicon/PQ Interaction

Under certain high temperature annealing conditions, the silicon (100) surface undergoes a $[2 \times 1]$ reconstruction to form rows of silicon “dimers” [83]. Each dimer consists of a Si-Si bond, with strong σ and weak π character [83, 84]. This gives the dimer a chemical behavior analogous to that of a C-C double bond, and it can participate in a $[4+2]$ cycloaddition (Diels-Alder-like reaction) with conjugated dienes [85].

A similar heteroatomic $[4+2]$ cycloaddition reaction was previously suggested between the carbonyl carbons (C=O) of PQ and the silicon dimers on the silicon (100) surface (Fig. 3.6) [77]. In this reaction the Si atoms are formally oxidized, and the PQ is formally reduced to a 9,10-dihydroxyphenanthrene adduct. Interestingly, the

π -electron conjugation of PQ, and hence its semiconducting property, is maintained in the reaction.

X-ray Photoelectron Spectroscopy (XPS)

Our work does not use a high temperature anneal prior to PQ deposition, so a $[2\times 1]$ reconstructed surface is not expected. Instead we start with an ill-defined hydrogen-passivated silicon (100) surface [78, 86]. To investigate the bonding between this surface and PQ, we measured the XPS spectra of the C 1s and Si 2p core levels using the Al $K\alpha$ line (1486.6 eV).

For the experiment, first a 10nm thin layer of PQ was deposited using Angstrom Evaporator in C405. Passivated samples were then transported in air to the UHV system in Prof. Kahn's lab. Typically samples were to no more than a 5 minutes in air during the transport.

The C 1s spectrum of PQ-passivated p-type silicon ($<0.005 \Omega \text{ cm}$), shown in Fig. 3.7 (solid line), can be decomposed into two components (dash-dot curves). The first peak at 284.7 eV is usually a signature of simple aromatic carbon atoms and can be attributed to the peripheral aromatic rings of PQ [77]. However, the binding energy of the second peak at 286.2 eV, is significantly lower than the 287.7–289.3 eV range typically associated with carbonyl group carbon atoms [77] and is in the range reported for typical phenolic carbons [87]. The shift in the binding energy of this second peak indicates that while the aromatic rings are intact, the carbonyl groups of PQ at the Si/PQ interface have been strongly modified by interacting with the underlying silicon surface. There are 12 aromatic and 2 carbonyl carbon atoms in the starting PQ molecule, so the aromatic carbon signal is expected to be six times (12/2) stronger than the carbonyl carbon signal (If we make the simplistic assumption that silicon is covered with a uniform monolayer of PQ). This compares well with the measured signal strength ratio (the area under the peaks) of 5.2:1 of the Si-bound

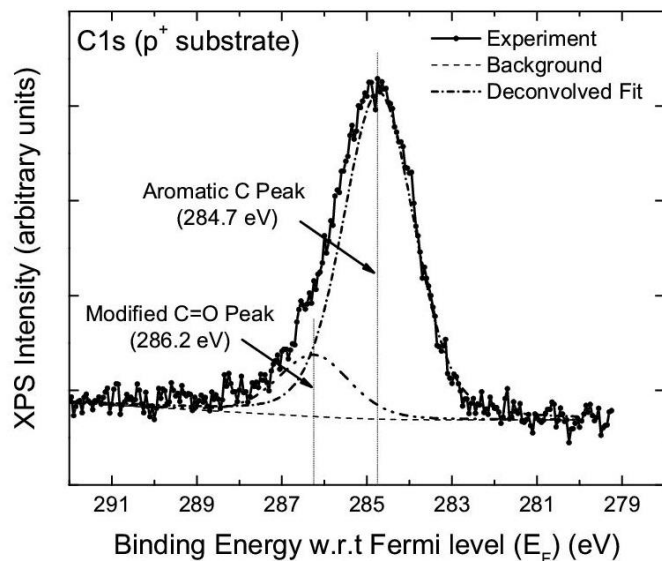


Figure 3.7: C 1s XPS spectrum for PQ-passivated highly-doped p-type silicon (100) surfaces. The data (black line) can be further resolved into 2 distinct peaks (dash-dot) at 284.7 eV and 286.2 eV. These peaks correspond to the binding energies of the aromatic C (C=C) and the phenolic-like (C=O) species of the bound PQ molecule, supporting the mechanism proposed in Fig. 3.4

species. All these results are congruent with the proposed cyclo-addition mechanism where the silicon atoms react exclusively with carbonyl groups of PQ (Fig. 3.4b) making them more phenoxy-like (Fig. 3.8).

The role of hydrogen that was initially attached to silicon is not clear. We suspect that the hydrogen breaks off from silicon and reduces the nearby C=C (note the difference in the final adduct of Fig. 3.6 and Fig. 3.8, the middle ring is not aromatic in the latter figure), but there is no evidence in support of or against the interaction.

While the exact structure of the underlying silicon surface is not known, any unreacted silicon valencies (“dangling” bonds) may lead to midgap defect states at the silicon surface. These states may carry charge, causing the bands at the surface to bend towards midgap. The amount of this surface band-bending (ΔE_{BB}) can be inferred from the position of the Si 2p peak in the XPS spectrum using the technique developed by Kraut *et al.* [88]. Note that the probing depth of XPS is deep enough

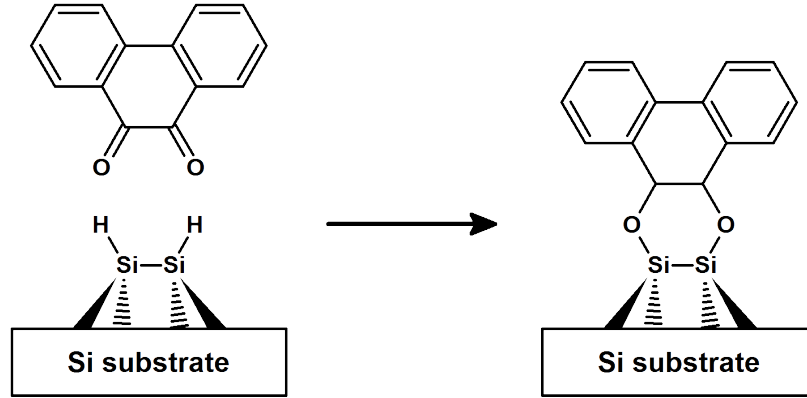


Figure 3.8: The reaction between 9,10-Phenanthrenequinone (PQ), the surface passivation precursor, and silicon as supported by the C 1s XPS results of Fig. 3.7. Unlike the reaction proposed by Fang *et al.* [77], we start with a ill-defined Si-H surface.

to allow measurement of the substrate Si 2p core level through the 10-nm-thick PQ layer [89]. Also the bulk of the Si 2p signal comes from the top few Si layers (4-6 layers corresponding to a depth of $\sim 2-3$ nm), where the band position is basically the same ($\pm 10-20$ meV) as at the very surface of the Si crystal.

We have previously measured the Si 2p peak to be 98.9 ± 0.1 eV below the Fermi-level (E_F) for a highly-doped p-type silicon wafers (p^+ , doping $> 10^{19}\text{cm}^{-3}$), known to have flat bands at the surface ($\Delta E_{BB} = 0$). Similar values of Si 2p binding energy have been reported previously [90]. In comparison, for a p^+ wafer that was cleaned and hydrogen-passivated as described above (but not PQ-passivated), the Si 2p peak was measured at 99.4 ± 0.1 eV below the Fermi-level (Fig. 3.9, top curve). This corresponds to a downward surface band-bending of 0.5 eV, presumably due to a large density of positively charged donor-like surface defects ($\Delta E_{BB} = 0.5$ eV). The presence of such defects at the hydrogen-passivated surface is not unexpected, as the “imperfection” of a wet-cleaned silicon (100) surface has been previously reported [78, 86].

PQ deposition reduces the amount of band-bending. A highly-doped p-type wafer onto which PQ was deposited, as per the method described above, shows the Si 2p peak at 99.1 ± 0.1 eV with respect to E_F (Fig. 3.9, middle curve), corresponding to a

band-bending of only 0.2 ± 0.1 eV. ($\Delta E_{BB} = 0.2$ eV). This 0.3 eV decrease of ΔE_{BB} is especially significant because the bands of heavily-doped silicon are very difficult to bend. The fact that the Fermi-level is pinned at midgap on a highly doped wafer indicates that the defect density is still high at the hydrogen-passivated surfaces. PQ-deposition substantially reduces the defect density, allowing the bands at the surface to bend less and the valence band edge to get closer to Fermi-level. This is consistent with the proposed mechanism (Fig. 3.4), according to which PQ reacts with and consumes the “dangling” bonds on the silicon surface.

The component corresponding to the Si-O bonding is not readily apparent in the Si 2p core level, even though Si-O bond is presumably present in PQ-passivated silicon as per the proposed mechanism (Fig. 3.4). There are two reasons for this lack of evidence. First, the shift in the Si 2p level expected for a Si-atom chemically bonded to three silicon atoms and one oxygen is only ~ 0.5 eV [91]. This shift is too small for the resolution of the XPS measurements performed in this work. Second, the intensity of the shifted component is expected to be small compared to the intensity of the unshifted Si core level. This is because only two Si atoms per PQ molecule contribute to the shifted signal, while the unshifted signal has contributions from many layers of subsurface Si atoms.

In a simple model that assumes a uniform surface donor-like defect density (D_{it} ; in $\text{cm}^{-2}\text{eV}^{-1}$) from midgap to valence band edge, the charge neutrality can be invoked to derive the relation between D_{it} and ΔE_{BB}

$$D_{it} = \sqrt{\frac{2\epsilon_s N_A \Delta E_{BB}}{q(E_G/2 - \Delta E_{BB})^2}} \quad (3.14)$$

where, ϵ_s is the silicon permittivity of silicon, E_G is the silicon bandgap, and N_A is the silicon doping. So in terms of surface defect density, the reduction of ΔE_{BB} due to PQ deposition implies a removal of $\sim 6 \times 10^{13}$ $\text{cm}^{-2}\text{eV}^{-1}$ defects from the silicon

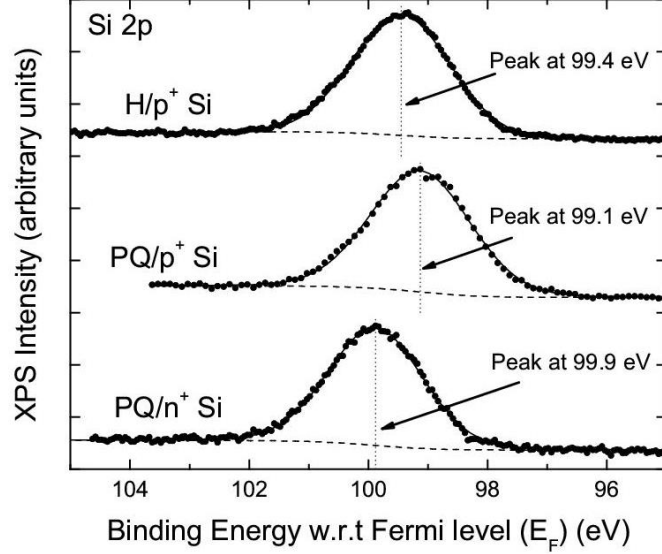


Figure 3.9: Si 2p binding energies (E_{2p}), w.r.t to bulk Fermi-level (E_F), of highly-doped silicon (100) surfaces. The three curves represent solution-processed H-passivated p-type surface (H/p⁺-Si), PQ-passivated p-type surface (p⁺-Si/PQ), and PQ-passivated n-type surface (n⁺-Si/PQ).

Table 3.2: The surface band-bending (ΔE_{BB}) in silicon for the three cases of Fig.3.9.

	$E_{2p} - E_F$ (eV)	ΔE_{BB} (eV)
Flat-band p ⁺ -Si	98.9 ± 0.1	0.0
H/p ⁺ -Si	99.4 ± 0.1	0.5
PQ/p ⁺ -Si	99.1 ± 0.1	0.2
Flat-band n ⁺ -Si ^a	100.0 ± 0.1	0.0
PQ/n ⁺ -Si	99.9 ± 0.1	-0.1

^ap⁺-Si at flatband + 1.1 eV

surface.

Though the lower band-bending suggests a reduction of the number of charged defects, the presence of neutral defects is still possible. For example, there might still be a high density of midgap acceptors that are neutral above the Fermi-level and hence do not cause band-bending on a p-type surface. To investigate this possibility, similar measurements were also done on highly-doped n-type (n⁺) surfaces. For PQ-passivated n⁺ wafers (Fig. 3.9, bottom curve) the Si 2p binding energy was $99.9 \pm$

0.1 eV. The expected difference in Fermi-level positions on p^+ and n^+ Si is 1.12 eV, so in the flat band condition, the n-type surface Si 2p core level should have a binding energy of 100.0 ± 0.1 eV. Comparing the two numbers, we estimate the surface band-bending on the PQ-passivated n^+ surfaces to be $0.1 \text{ eV} \pm 0.1 \text{ eV}$ ($\Delta E_{BB}=0.1 \text{ eV}$). The difference in Si 2p binding energies between the p^+ and n^+ silicon surfaces ($99.9 - 99.1 = 0.8 \text{ eV}$) is the range of surface energies over which the Fermi-level may be modulated. These measurements imply a relatively small number of deep surface states, and agree with the minority-carrier lifetime results, where we extracted low recombination velocities ($\sim 150 \text{ cm/s}$) at the PQ-Si interface.

Ultra-violet and Inverse Photoelectron Spectroscopy

A distinct advantage of using PQ-passivation over traditional passivating layers like silicon-dioxide, which is an insulator, is the possibility for current-conduction across the Si/PQ interface. The conjugated π bonds of PQ suggest that it is a semiconducting molecule and hence it can transport charge more efficiently. For a more thorough evaluation of the electrical conduction properties of PQ, the highest occupied molecular orbital (HOMO) and the lowest unoccupied molecular orbital (LUMO), were determined by UPS and IPES. Together with the XPS results, these techniques provide an accurate determination of the alignment between the PQ and Si energy levels at the interface. Measurements were taken on both highly-doped p and n-type silicon surfaces.

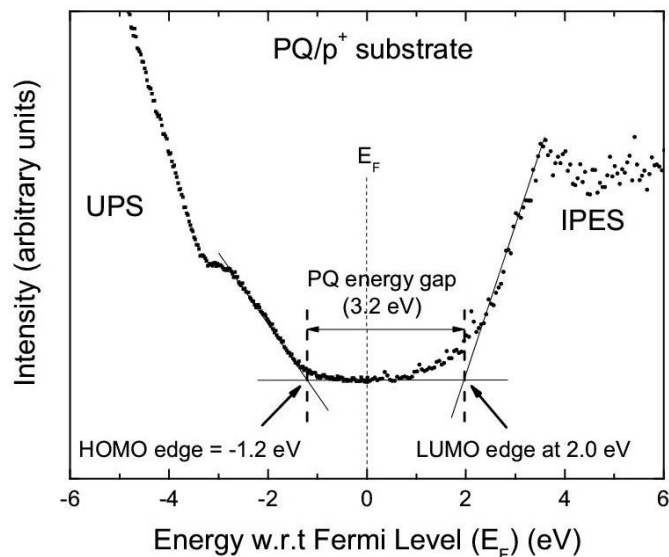
The UPS measurements used the He I line (21.22 eV) of a gas discharge source, and IPES used a commercial electron gun and a fixed photon energy detector (centered at 9.2 eV), the details of which have been published elsewhere [92]. The resolution of the UPS and IPES measurements was estimated at 0.15 and 0.45 eV, respectively. The energy scales of the UPS and IPES spectra were aligned by measuring the position of the Fermi edge with both techniques on freshly evaporated Au films.

The UPS and IPES spectra for a PQ layer on p⁺ Si are shown in Fig. 3.10(a). In the UPS spectrum, the signal at the lowest binding energy corresponds to the electrons photoemitted from the top of the filled states at the surface [93]. Due to the thickness of the PQ overlayer (10 nm) the signal from the Si valence band is assumed to be entirely suppressed. Thus the edge closest to zero gives the HOMO edge of the bound PQ molecule on the passivated p⁺ Si at 1.2 eV below the Fermi-level. Similarly, in the IPES spectrum, the signal at the lowest binding energy corresponds to the bottom of the empty states, i.e. the edge of bound PQ LUMO [93]. On PQ-passivated p⁺ Si, the LUMO edge is at 2.0 eV above the Fermi-level. Hence, the HOMO-LUMO difference, i.e. the energy gap, of PQ is 3.2 eV.

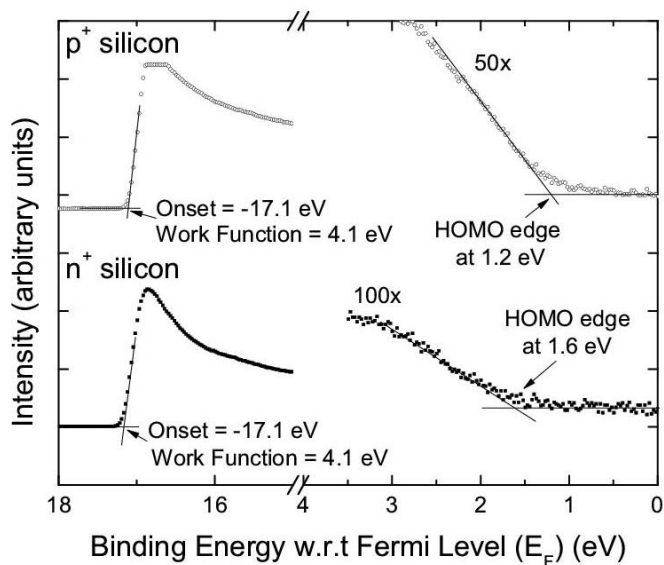
The UPS signal at the highest binding energies (labeled as onset in Fig. 3.10(b)) corresponds to the photoemission cut-off from which vacuum level and the work function (Φ) are extracted [93]. For the PQ-passivated p⁺ Si, $\Phi = 4.1$ eV. Based on these results, the ionization energy (IE) and electron affinity (χ) of PQ-passivated p⁺ Si can be determined to be 5.3 eV and 2.1 eV, respectively. These numbers are consistent with a first-principles calculations reported in literature [94].

Typically, for a $\sim 10^{19}$ cm⁻³ doped p-type silicon with negligible band bending, the Φ , ionization energy and electron affinity are of the order of 5.2, 5.2 eV and 4.0 eV, respectively [95]. Together with the ~ 0.2 eV band-bending in Si (calculated by XPS as described above), this allows us to calculate the band alignment at the Si/PQ interface. Overall, the PQ-p⁺ Si interface is a type-I heterojunction, as detailed in Fig. 3.11a. There is a 1.1 eV band-offset at the conduction band and a 1.0 eV band-offset at the valence band. Results for PQ-n⁺ Si interface are similar (Fig. 3.11b), but the implied values of the band-offsets at the conduction and valence band are 1.4 eV and 0.6 eV, respectively.

Finally, a clarification note: this study does not differentiate between the band structure of PQ bonded to silicon and bulk PQ that just sits on the top. A more



(a)



(b)

Figure 3.10: (a) Composite He I (21.22 eV) UPS and IPES of PQ-passivated highly-doped p-type silicon (100) surface. (b) UPS spectra of PQ-passivated highly-doped p- and n-type silicon (100) surfaces showing the onset. The resulting band-diagram is shown in Fig. 3.11.

detailed study that tracks the band-structure of the surface, from pristine silicon to multiple monolayers of PQ on silicon, may be insightful.

An interesting, but not well understood, observation is the presence of an interface dipole at the PQ/p⁺-Si interface. It can be quite large and depends on the

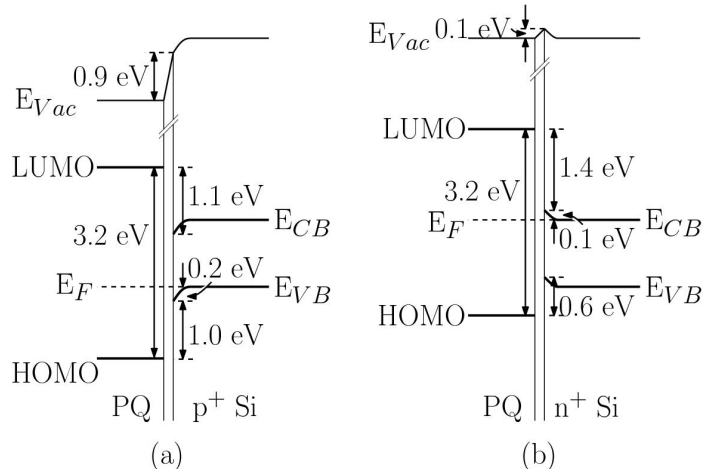


Figure 3.11: Band offsets at the Si/PQ Interface: The band diagram of the PQ-passivated silicon surface for highly doped (a) p-type and (b) n-type silicon (100) surfaces. The band-bending in silicon is extracted from the XPS data (Fig. 3.9). The offsets at Si/PQ heterojunction have been extracted from the UPS and IPES data (Fig. 3.10b, Fig. 3.10a). In both cases and interface dipole is measured.

Si work function, from 0.9 eV for p^+ to 0.1 for n^+ Si. The presence of interface dipoles at organic/silicon interfaces that depend on the work-function of the underlying substrates, have been previously observed for a number of metal/organic interfaces [96, 97], and a number of mechanisms have been proposed to explain their origin [98]; for example charge transfer between the chemisorbed organic and underlying metal [97]. The origin of the dipole at the Si/PQ interface, and its dependence on silicon doping (or equivalently, the silicon work-function) could be similar. For a more exact explanation a more detailed analysis of the phenomenon is needed.

In summary, the spectroscopy reveals that PQ reacts with the silicon surface via the C=O. The band-bending at PQ-passivated Si surface is lower than H-passivated silicon surface, suggesting a lower defect density at PQ-passivated surfaces. Finally, the energy-gap of PQ is 3.2 eV, and it forms a wide-bandgap type-I heterojunction with silicon with large offsets at both conduction and valence band of silicon.

3.7 Field-Effect Devices

3.7.1 Metal-Insulator-Semiconductor Capacitor

A test of a semiconductor surface with low defect density is the ability to modulate the Fermi-level. To demonstrate the quality of the PQ-silicon interface, we fabricated metal/insulator/semiconductor capacitors (MISCap) on PQ-passivated silicon wafers. For comparison, a control structure with the same cleaning steps but without the PQ passivation was also fabricated along with the PQ-passivated sample. The structure consists of lightly doped p-type PQ-passivated silicon wafers coated with a layer of an insulating polymer resin (Photoresist AZ5214) and aluminum (Al) (Fig. 3.12(a)). The resin is selected as the insulator due to its low-temperature deposition (4000 rpm spin-coating followed by a bake at 95 °C in vacuum oven) and lack of any aggressive chemistry with silicon or PQ. The gate metal was deposited by thermal evaporation through a 1-mm radius shadow mask.

The small-signal capacitance-voltage characteristics of these structures, measured at a frequency of 1 MHz and a DC-bias step rate of ~ 0.25 V/s, are shown in Fig. 3.12(b). Without PQ the capacitance is fixed, presumably due to the large density of defects which makes it impossible to bend bands at the silicon surface. On the other hand with PQ, the measured characteristic is typical of a metal/insulator/semiconductor system: the larger flat capacitance at negative voltages denoting accumulation, and the decreasing capacitance at positive voltages denoting depletion (and possibly inversion). Similar results are also obtained for capacitors fabricated on n-type silicon wafers (Fig. 3.12(c) & (d)), although the evidence for an inversion layer is slightly tenuous.

The large hysteresis in the data is probably due to charge trapping in the low-temperature insulator and not due to silicon surface defect density, a fact confirmed by the high carrier mobilities obtained in the field-effect transistors with the same

MIS structure (see next section).

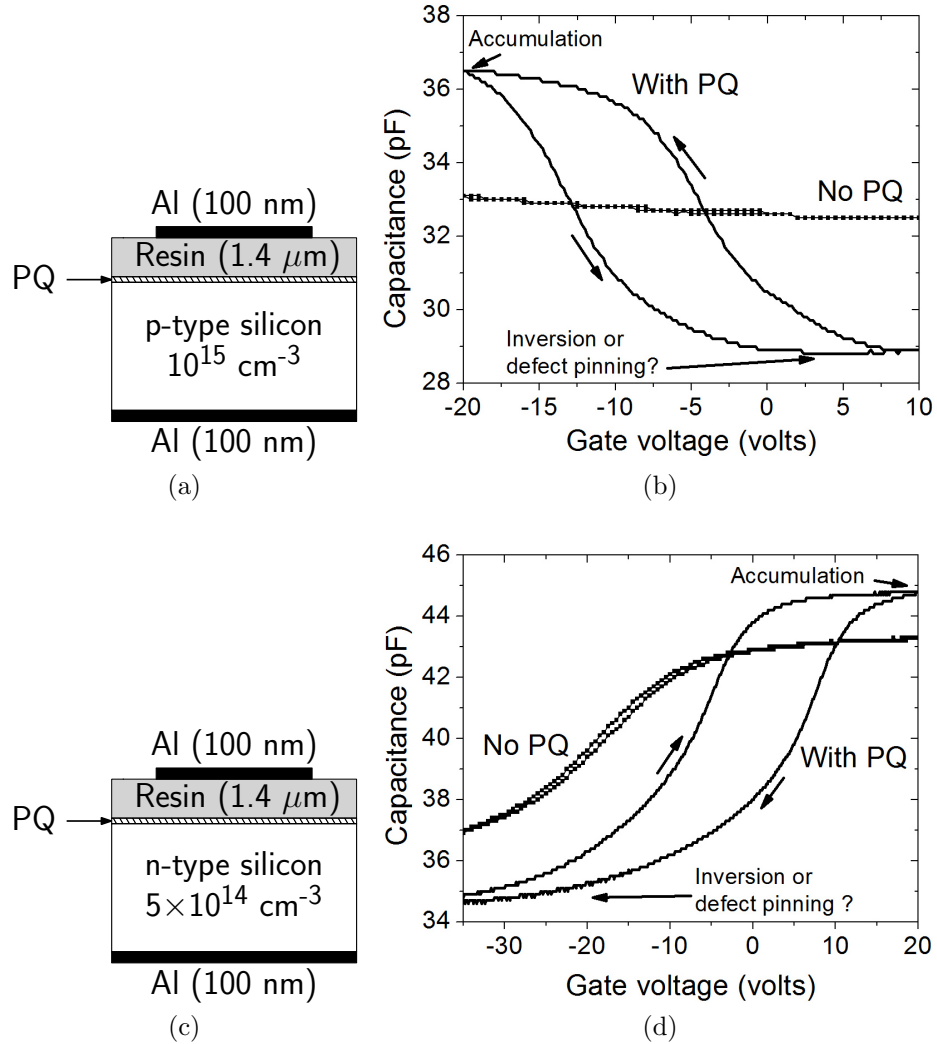


Figure 3.12: (a) PQ passivated metal-insulator-semiconductor capacitor structure on p-type silicon. The insulator is AZ5124 polymer resin. (b) The small-signal capacitance at 1 MHz of a metal-insulator-semiconductor capacitor. (c) Similar metal-insulator-semiconductor capacitor structure on n-type silicon and (d) its small-signal capacitance at 1 MHz.

3.7.2 Metal-Insulator-Semiconductor Field-Effect Transistor

While the clear presence of accumulation and depletion in the capacitance-voltage characteristics confirms that at the PQ-passivated surface the Fermi-level can be modulated, it does not conclusively prove inversion in silicon. The characteristics

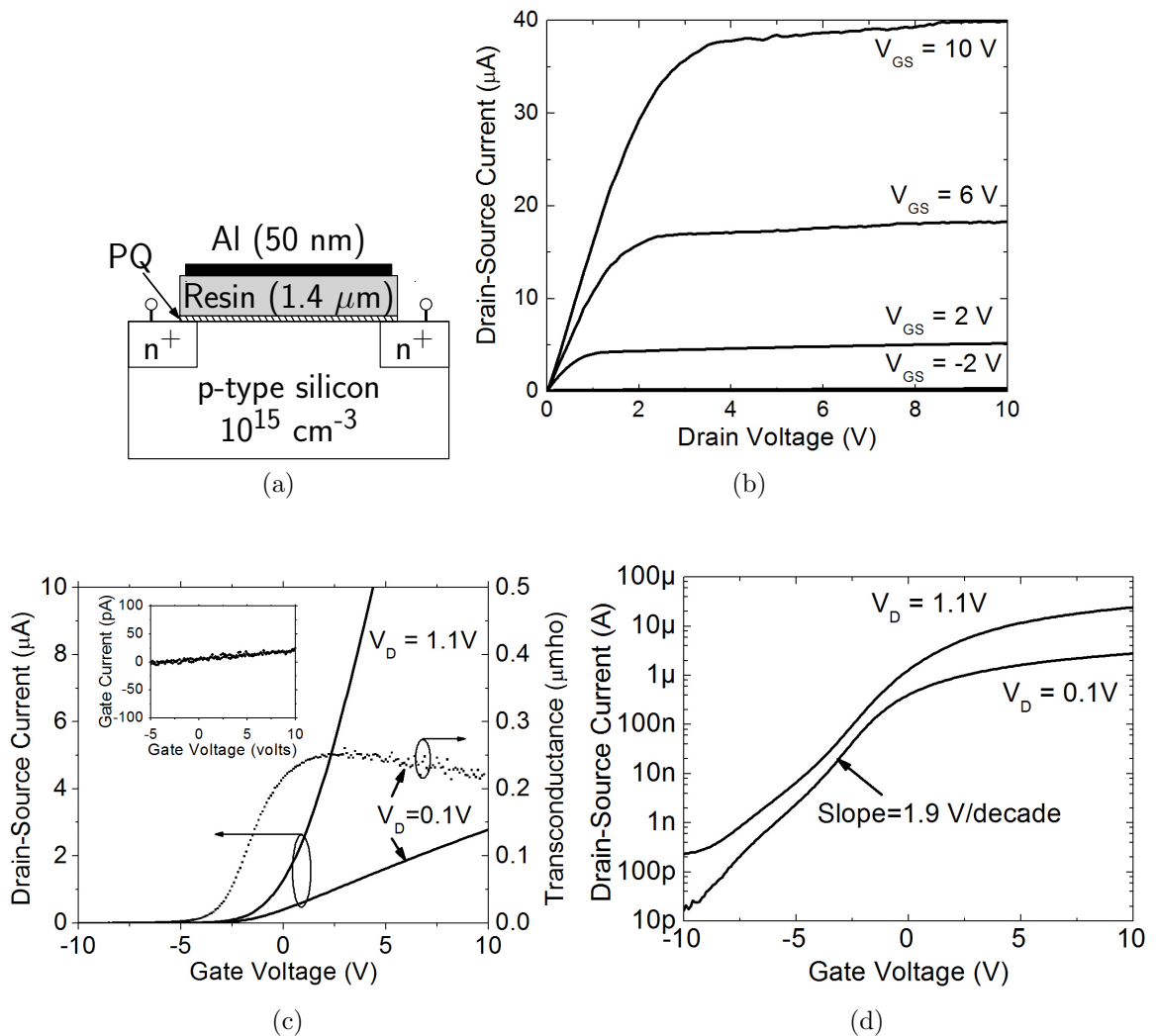


Figure 3.13: (a) The n-channel metal-insulator-semiconductor field-effect transistor structure. The L and W of the devices are $\sim 1 \text{ mm}$ and $\sim 1.91 \text{ mm}$, respectively. (b) Drain current vs. drain voltage characteristics at different gate voltages (V_{GS}). (c) Drain current and transconductance vs. gate voltage characteristics at different low drain voltages in linear and (d) log scale.

would be very similar if a large density of acceptor-like defect states are pinning the Fermi-level before actual inversion is reached [99].

To test for true inversion, n-channel metal-insulator-semiconductor FET (MISFET) devices were fabricated with a PQ/insulator stack on light-doped p-type substrates (Fig. 3.13(a)). The source and drain are formed *before* the deposition of either PQ or the organic insulator, by a conventional process - high-dose phosphorous ion

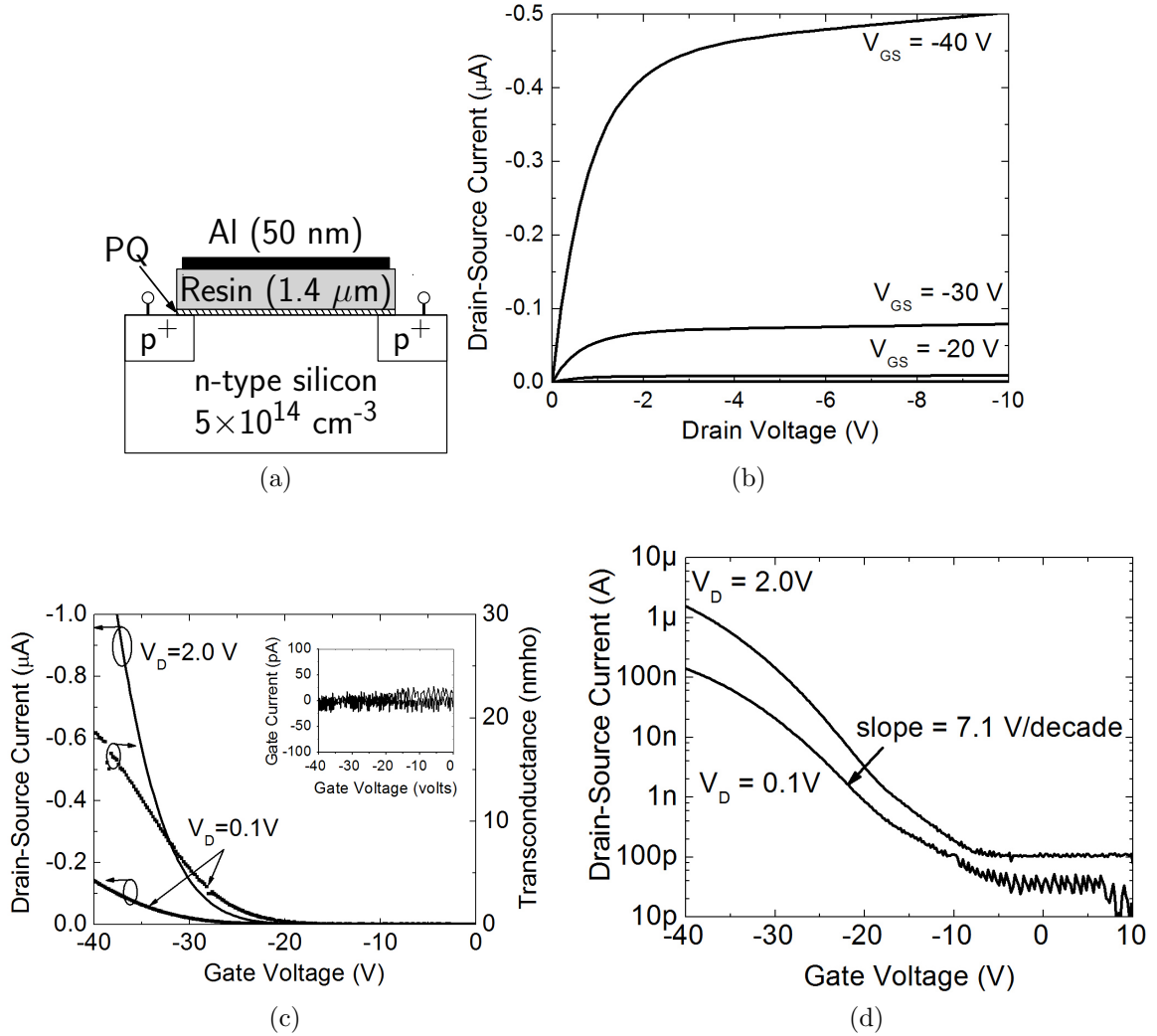


Figure 3.14: (a) The p-channel Metal-insulator-semiconductor field-effect transistor structure. The L and W of the devices are $\sim 1 \text{ mm}$ and $\sim 1.91 \text{ mm}$, respectively. (b) Drain current vs. drain voltage characteristics at different gate voltages (V_{GS}). (c) Drain current and transconductance vs. gate voltage characteristics at different low drain voltages in linear and (d) log scale.

implantation (10^{16} cm^{-2} at 100 keV) followed by a $900 \text{ }^\circ\text{C}$ anneal in nitrogen ambient. Next PQ and the insulating resin were deposited on silicon, using the same recipe as in previous sections. No source/drain metal contacts were evaporated. During measurement, contact to the source and drain regions was made by jamming a sharp probe into the source/drain regions of silicon, through the soft insulating organic resin. As with the MISCap structure, gate metal was thermally evaporated via a

1-mm radius shadow-mask, overlapping the source/drain regions.

Measurements reveal well-behaved n-channel MISFET characteristics which convincingly show an “inversion” layer of mobile electrons (Fig. 3.13(b)-(d)). The gate leakages were <25 pA for a gate-bias of <10 V. As a control, conventional MOS transistors were also used, in which a high-quality thermal oxide was used as the gate dielectric and for surface passivation. The current-voltage characteristics of these p-channel and n-channel MOSFETs are shown in Appendix C.

Qualitatively, similar results are also obtained for p-channel MISFET devices (Fig. 3.14). The source and drain in this case were also formed before the deposition of either PQ or the organic insulator, but with high-dose boron ion implantation (10^{16}) cm^{-2} at 100 keV) and 900 °C anneal.

The sub-threshold slope (S) of a FET device depends on the interface defect density (D_{it} , in $\text{cm}^{-2}\text{eV}^{-1}$) according to the relation

$$S \text{ (mV/decade)} = 60 \left(1 + \frac{q^2 D_{it}}{C_i} \right) \quad (3.15)$$

where C_i is the gate capacitance per unit area. From the accumulation capacitance in MISCap characteristics (Fig. 3.12), the value of C_i is estimated to be ≈ 1 nF/ cm^2 . The sub-threshold slope of the n-channel FET is 1900 mV/decade (Fig. (d)), so at the p-Si/PQ interface, the implied interface defect density is $\sim 2 \times 10^{11}$ $\text{cm}^{-2}\text{eV}^{-1}$. Similarly from the p-channel FET, the implied interface trap density is $\sim 1 \times 10^{12}$ $\text{cm}^{-2}\text{eV}^{-1}$. These values are in the same ball-park with surface defect density calculated from the surface recombination velocity.

The drain-source current (I_{DS}) of a metal-insulator-semiconductor field effect transistor, in the linear region ($V_{DS} \ll V_{GS} - V_T$ and $V_{GS} > V_T$), is given by the well known equation

$$I_{DS} = \frac{W}{L} \mu_0 C_i \left[(V_{GS} - V_T) V_{DS} - \frac{V_{DS}^2}{2} \right] \quad (3.16)$$

where W is the channel width, L is the channel length, V_T is the threshold voltage and V_{GS} and V_{DS} the gate and drain voltages with respect to the source, respectively. To calculate mobility, a C_i of 1.1 - 1.4 nF/cm² is estimated from the accumulation capacitance of the metal-organic-insulator-semiconductor capacitor (Fig. 3.12). The L for the devices is ~ 1 mm, but due to a circular gate shape (Fig. 3.15(a)) the value of W is not obvious. Considering the active channel area under the gate is 1.91 mm², we estimate an effective W of ~ 1.91 mm.

There are several ways to extract a mobility value from FET data [100, 101] from the Eq.(3.16). One value of mobility, referred to as the effective mobility (μ_{eff}), can be calculated from the I_D versus V_{GS} characteristics at low V_{DS} , given by the equation

$$\mu_{eff} = \frac{I_D}{V_{DS}} \frac{L}{W} \frac{1}{C_i(V_{GS} - V_T)} \Big|_{V_{DS} \rightarrow 0} \quad (3.17)$$

The main drawback of this approach is that the value of V_T needs to be approximated [101]. Alternatively, the field-effect mobility (μ_{FE}) can be calculated from the transconductance ($g_m = \frac{\partial I_{DS}}{\partial V_{GS}}$) at low V_{DS} using

$$\mu_{FE} = \frac{L}{W} \frac{g_m}{C_i V_{DD}} \Big|_{V_{DS} \rightarrow 0} \quad (3.18)$$

Electron mobility for the n-channel device versus excess gate voltage ($V_{GS} - V_T$) is shown in Fig. 3.15(c). A peak electron field-effect mobility of ~ 640 cm²/Vs is extracted from the drain current vs. gate voltage characteristic at a drain voltage of 0.1 V. The mobility is four times higher than what was previously reported for a crystalline silicon FET with an organic gate dielectric [102], and is similar to our control device with a thermally-grown silicon dioxide as the insulator (Fig. 3.15(d)). The extracted hole mobility from p-channel device is ~ 50 cm²/Vs (Fig. 3.15(e)) is lower than the control device as compared to 225 cm²/Vs measured on the control device (Fig. 3.15(f)), probably reflecting the higher defect-density that was extracted

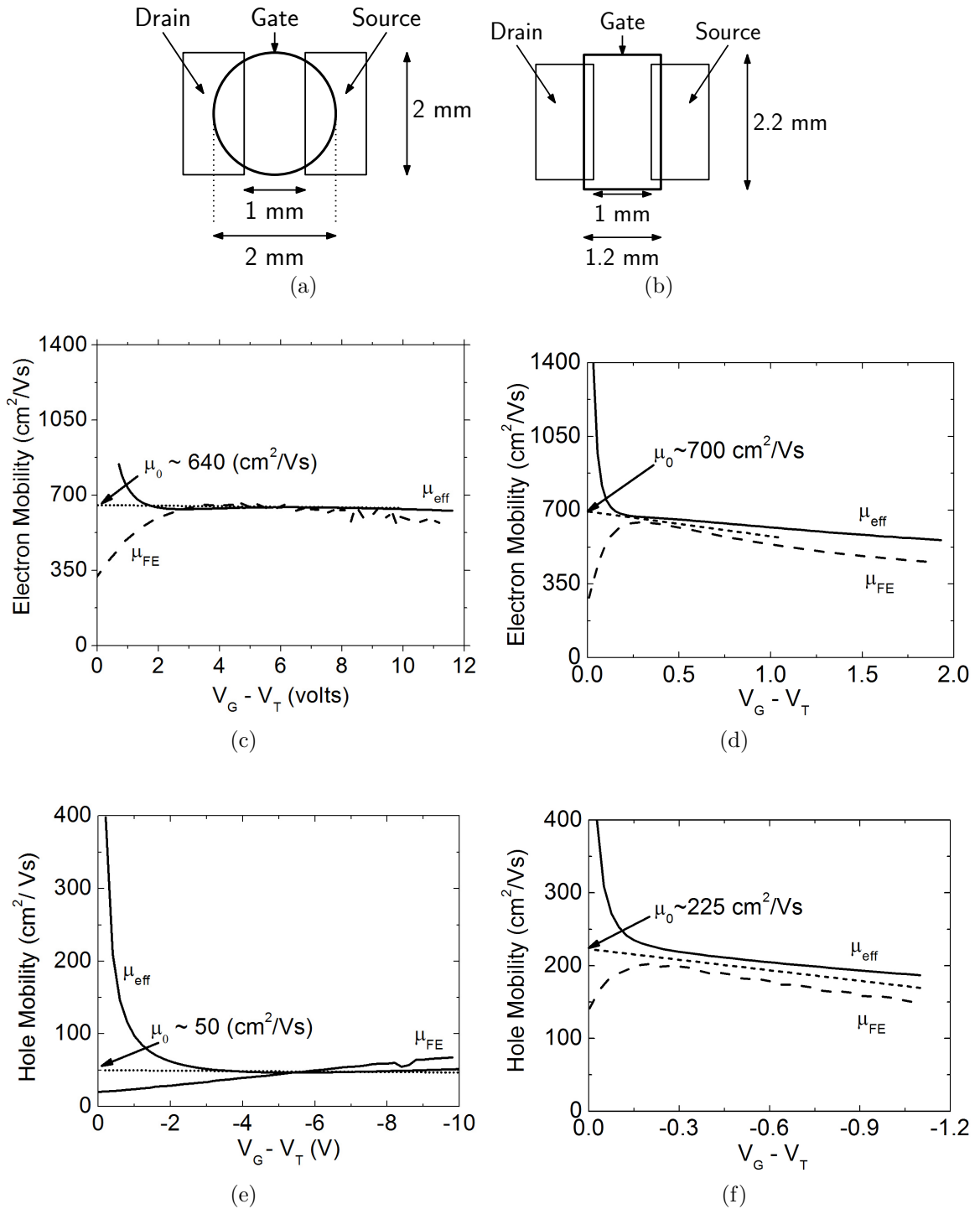


Figure 3.15: The top view of the FET devices showing the dimensions of the gate (a) for PQ-passivated MISFET (a) for conventional MOSFET (Control). Extracted carrier mobility from (c) n-channel MISFET, (d) n-channel MOSFET, (e) p-channel MISFET, and (f) p-channel MOSFET.

from the sub-threshold slope. Still, these mobilities are high for silicon surfaces that were passivated at room-temperature, proving two things a) the PQ-silicon interface Fermi-level can indeed be modulated from mid-gap to the conduction band edge and b) the Si/PQ interface is of very high electronic quality, i.e. interface defect density is low. These assertions are highly consistent with the spectroscopic and minority-carrier recombination data presented above.

A interesting question arising from the MISFET results is - where are the electrons in the inversion layer localized, silicon or PQ? If we are to assume, for the sake of argument, that the inversion-layer electrons are localized in the organic PQ, and not Si, the expected mobilities would be far lower and more in line with mobilities of organic FETs (typically $< 10 \text{ cm}^2\text{V}^{-1}\text{s}^{-1}$) [103, 104]. The fact that we see mobilities that are two orders of magnitude higher and comparable to crystalline Si FETs, strongly suggests that this is not that case. The band-alignment data of Fig. 3.11a provides the precise explanation. In an n-channel FET, the bands of p-Si bend down under positive gate-bias to form a thin layer of mobile electron in Si (the “inversion” layer) at the insulator/Si interface. However, the electron-barrier at the PQ/p-Si interface, between the conduction band (CB) minimum of Si and the LUMO of PQ, is quite significant (1.1 eV). In PQ-passivated p-Si, the inversion layer electrons are blocked by this barrier from getting into the PQ layer.

3.8 Conclusion

The passivation of the silicon (100) surface using the organic molecules 9-10 phenanthrenequinone was demonstrated. Very low surface recombination velocities are measured at PQ-passivated silicon surfaces. Spectroscopy tests reveal the passivation mechanism - PQ chemically bonds to the silicon (100) surface atoms, and in the process consumes the “dangling” bonds typically found on bare Si surfaces. Band-

bending is greatly reduced at both n- and p-type silicon surfaces. This implies low densities of both acceptor and donor-like defects at the interface. The Si/PQ interface is not insulating, rather the alignment of the energy levels is such that PQ forms a wide-bandgap type-I heterojunction with silicon. Furthermore, the Fermi-level at PQ-passivated Si is not pinned, and can be modulated across the band gap. High carrier mobilities are obtained in field-effect transistors, further confirming the low surface defect densities.

These results are promising and could provide a way to integrate organic materials with silicon to form hybrid organic/silicon electronic devices. PQ was selected for this study due to its unique chemical properties [77] and easy commercial availability. One might expect that with a systematic approach and tailored molecules even better passivating organic molecules can be found.